

## Dependence of $X_{\text{CO}}$ on metallicity, intensity, and spatial scale in a self-regulated interstellar medium

CHIA-YU HU (胡家瑜)<sup>1</sup>, ANDREAS SCHRUBA<sup>1</sup>, AMIEL STERNBERG<sup>2,3,1</sup> AND EWINE F. VAN DISHOCK<sup>1,4</sup>

<sup>1</sup>*Max-Planck-Institut für Extraterrestrische Physik, Giessenbachstrasse 1, D-85748 Garching, Germany*

<sup>2</sup>*School of Physics & Astronomy, Tel Aviv University, Ramat Aviv 69978, Israel*

<sup>3</sup>*Center for Computational Astrophysics, Flatiron Institute, 162 5th Ave, New York, NY 10010, USA*

<sup>4</sup>*Leiden Observatory, Leiden University, P.O. Box 9513, NL-2300 RA Leiden, the Netherlands*

### ABSTRACT

We study the CO(1–0)-to-H<sub>2</sub> conversion factor ( $X_{\text{CO}}$ ) and the line ratio of CO(2–1)-to-CO(1–0) ( $R_{21}$ ) across a wide range of metallicity ( $0.1 \leq Z/Z_{\odot} \leq 3$ ) in high-resolution ( $\sim 0.2$  pc) hydrodynamical simulations of a self-regulated multiphase interstellar medium. We construct synthetic CO emission maps via radiative transfer and systematically vary the “observational” beam size to quantify the scale dependence. We find that the kpc-scale  $X_{\text{CO}}$  can be over-estimated at low  $Z$  if assuming steady-state chemistry or assuming that the star-forming gas is H<sub>2</sub>-dominated. On parsec scales,  $X_{\text{CO}}$  varies by orders of magnitude from place to place, primarily driven by the transition from atomic carbon to CO. The pc-scale  $X_{\text{CO}}$  drops to the Milky Way value of  $2 \times 10^{20} \text{ cm}^{-2} (\text{K km s}^{-1})^{-1}$  once dust shielding becomes effective, independent of  $Z$ . The CO lines become increasingly optically thin at lower  $Z$ , leading to a higher  $R_{21}$ . Most cloud area is filled by diffuse gas with high  $X_{\text{CO}}$  and low  $R_{21}$ , while most CO emission originates from dense gas with low  $X_{\text{CO}}$  and high  $R_{21}$ . Adopting a constant  $X_{\text{CO}}$  strongly over- (under-)estimates H<sub>2</sub> in dense (diffuse) gas. The line intensity negatively (positively) correlates with  $X_{\text{CO}}$  ( $R_{21}$ ) as it is a proxy of column density (volume density). On large scales,  $X_{\text{CO}}$  and  $R_{21}$  are dictated by beam averaging, and they are naturally biased towards values in dense gas. Our predicted  $X_{\text{CO}}$  is a multivariate function of  $Z$ , line intensity, and beam size, which can be used to more accurately infer the H<sub>2</sub> mass.

*Keywords:* Interstellar medium (847); Astrochemistry (75); Hydrodynamical simulations (767)

### 1. INTRODUCTION

Molecular clouds are the site for star formation. Characterizing how they form from, and interact with, the diffuse interstellar medium (ISM) is crucial for our understanding of galaxy evolution (Lada & Lada 2003; McKee & Ostriker 2007; Tacconi et al. 2020). However, molecular hydrogen (H<sub>2</sub>), the main component of molecular clouds, does not emit radiation under typical conditions. In contrast, carbon monoxide (CO), the second most abundant molecular species, is a very efficient emitter at low temperatures and therefore is the most commonly used tracer for H<sub>2</sub>. The CO-to-H<sub>2</sub> conversion factor

$$X_{\text{CO}} \equiv \frac{N_{\text{H}_2}}{W_{10}}, \quad (1)$$

is used to convert the observed intensity of the CO(1–0) line intensity ( $W_{10}$ ) to the H<sub>2</sub> column density ( $N_{\text{H}_2}$ ). The typical value found in the Milky Way is

$$X_{\text{CO,MW}} = 2 \times 10^{20} \text{ cm}^{-2} (\text{K km s}^{-1})^{-1} \quad (2)$$

within  $\pm 30\%$  uncertainty (see Bolatto et al. 2013 for a detailed review).

However, CO is not a perfect tracer for H<sub>2</sub>. Even at solar metallicity, CO is photodissociated deeper into the cloud by the far-ultraviolet (UV) radiation compared to H<sub>2</sub> (van Dishoeck & Black 1988; Sternberg & Dalgarno 1995), leading to a regime where H<sub>2</sub> gas is deficient in CO, commonly referred to as the “CO-dark” molecular gas (Wolfire et al. 2010). Furthermore, at low metallicities, the far-UV radiation progressively photodissociates more CO but only mildly so the H<sub>2</sub> (Madden et al. 1997; Pak et al. 1998; Bolatto et al. 1999; Wolfire et al. 2010), which expands the range of column densities where gas is CO-dark and leads to a higher  $X_{\text{CO}}$ , making CO a poor tracer of H<sub>2</sub>. Indeed, observations of nearby low-metal-

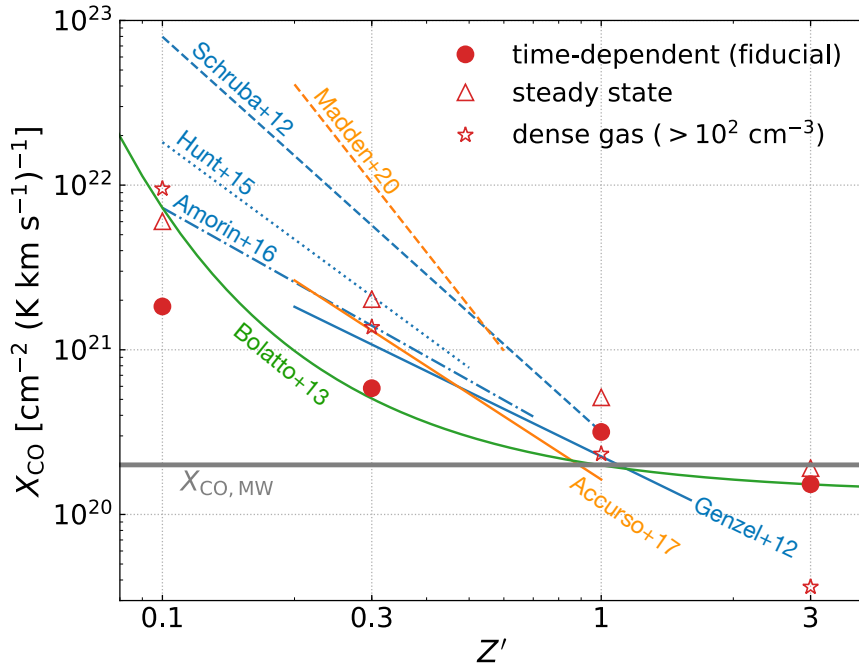


**Figure 1.** CO-to-H<sub>2</sub> conversion factor ( $X_{\text{CO}}$ ) as a function of normalized metallicity ( $Z' \equiv Z/Z_{\odot}$ ). The colored lines are from different observational studies as follows (showing only the dynamical range of  $Z'$  in each observation). Genzel et al. (2012): high-redshift ( $z > 1$ ) star-forming galaxies (inverse KS method); Schruba et al. (2012): dwarf galaxies (inverse KS method); Hunt et al. (2015): dwarf galaxies (inverse KS method); Amorín et al. (2016): blue compact dwarf galaxies (inverse KS method); Accurso et al. (2017): local star-forming galaxies (spectral synthesis method); Madden et al. (2020): dwarf galaxies (spectral synthesis method). The green solid curve shows the theoretical prescription from Bolatto et al. (2013). The horizontal grey line shows the standard Milky Way value (see Eq. (2)). The red symbols show the time-averaged global (1 kpc<sup>2</sup>)  $X_{\text{CO}}$  in our simulations (see Section 3.1). Red filled circles: our fiducial, time-dependent model; red non-filled triangles: the steady-state model; red non-filled stars: the “dense gas” conversion factor  $X_{100} \equiv N_{\text{H}}(n > 100 \text{ cm}^{-3})/W_{10}$ . Our time-dependent model can be described by Eq. (8). At low  $Z'$ ,  $X_{\text{CO}}$  can be overestimated both by the spectral synthesis method (by assuming steady-state chemistry) and by the inverse KS method (by assuming the star-forming gas is fully molecular).

licity dwarf galaxies have found that the CO emission is extremely weak (often undetectable), and the ratio of the total star formation rate (SFR) to the CO luminosity is much higher than what is found in typical spiral galaxies (Schruba et al. 2012; Cormier et al. 2014). If we assume that the ratio of total SFR to H<sub>2</sub> mass is insensitive to metallicity, this implies an elevated  $X_{\text{CO}}$  at low metallicities. Therefore, theoretical expectations and observations both suggest that  $X_{\text{CO}}$  increases at lower metallicity.

Observational measurements of  $X_{\text{CO}}$  are challenging as they require not only a successful CO detection (which is difficult at low metallicities) but also an independent method to derive the H<sub>2</sub> mass. The existing techniques include the following: (1) The inverse Kennicutt–Schmidt (KS) method (Genzel et al. 2012; Schruba et al. 2012; Hunt et al. 2015; Amorín et al. 2016) measures the SFR which is converted to the associated H<sub>2</sub> mass via an adopted correlation between the two quantities (i.e., the KS relation). (2) The dust-based method (Leroy et al. 2011; Elmegreen et al. 2013;

Shi et al. 2015; Lee et al. 2015; Schruba et al. 2017) uses infrared (IR) continuum measurements to derive the dust mass, which is converted to the total gas mass with an assumed dust-to-gas ratio (DGR). The H<sub>2</sub> mass is then derived by subtracting the atomic hydrogen (HI) mass (obtained through 21 cm emission) from the total gas mass. (3) The virial method (Bolatto et al. 2008; Rubio et al. 2015; Schruba et al. 2017) measures the CO line width and the cloud size to derive the H<sub>2</sub> mass assuming that clouds are in virial equilibrium. (4) The spectral synthesis method (Accurso et al. 2017; Madden et al. 2020) measures the fine structure “metal” lines (e.g. [C II] 158  $\mu\text{m}$ ) in addition to the CO(1–0) line, and uses chemistry and spectral synthesis codes with assumed cloud geometry to constrain the physical parameters of the ISM and derive the H<sub>2</sub> mass. Each of these methods relies on different assumptions that are mostly calibrated at solar metallicity, and their validity at low metallicities remains unclear. Therefore, it is perhaps not too surprising that there are still significant discrepancies on the  $Z$ – $X_{\text{CO}}$  relation derived

from different observations (see Fig. 1). On the other hand, the discrepancies may also indicate secondary dependencies. For example, the  $Z$ - $X_{\text{CO}}$  relation appears to be steeper in dwarf galaxies than in more massive, star-forming galaxies in Fig. 1.

Recently, high-resolution observations with the Atacama Large Millimeter/submillimeter Array (ALMA) have successfully detected CO at  $Z' \equiv Z/Z_{\odot} \sim 0.1$  and shown that CO typically originates from compact regions of a few parsecs (Rubio et al. 2015; Shi et al. 2015; Schrubba et al. 2017). More importantly, the  $X_{\text{CO}}$  derived from the virial method is found to be comparable to the Milky Way value and is significantly lower than the  $X_{\text{CO}}$  of the same targets derived from the dust-based method. This suggests a dependence on spatial scale (i.e., the beam size) as the high-resolution virial method measures  $X_{\text{CO}}$  in the compact (pc-scale), CO-bright cores while the dust-based method, which typically has a much larger beam size ( $\gtrsim 100$  pc), measures  $X_{\text{CO}}$  averaging over entire molecular clouds (or associations), including both CO-bright and CO-dark gas. However, the fundamental small-scale distribution of  $X_{\text{CO}}$ , which dictates  $X_{\text{CO}}$  on different (larger) scales, is still poorly understood. The main goal of this paper is to shed light on this subject in a systematic way.

Meanwhile, the CO(2–1) line has become more widely used as an alternative to CO(1–0) in recent years. For example, the recent high-resolution survey of nearby star-forming galaxies, PHANGS–ALMA (Leroy et al. 2021), chose CO(2–1) over CO(1–0) for better sensitivity. In this case, inferring  $\text{H}_2$  requires a two-step process: the observed CO(2–1) line intensity ( $W_{21}$ ) is first converted into  $W_{10}$  with an adopted line ratio

$$R_{21} \equiv \frac{W_{21}}{W_{10}}, \quad (3)$$

and then converted into  $N_{\text{H}_2}$  with an adopted  $X_{\text{CO}}$ . Understanding how  $R_{21}$  varies with ISM properties is therefore important for CO(2–1) to be used as an alternative  $\text{H}_2$  tracer (den Brok et al. 2021). Ultimately, for high-redshift galaxies, a similar method may be needed for CO lines of higher rotational levels.

Hydrodynamical simulations have been the theoretical frontiers of forward modeling the ISM structure, chemistry, and the observed line intensities. However, earlier studies have fundamental limitations in their setup. On small scales, cloud simulations (e.g., Glover & Mac Low 2011; Shetty et al. 2011a,b; Glover & Clark 2012a; Bisbas et al. 2017; Peñaloza et al. 2017, 2018; Bisbas et al. 2021) provide detailed information with very high resolution ( $\lesssim 0.1$  pc) but rely on unrealistic boundary conditions (e.g., isolated clouds) and artificial forces for

turbulence driving. In addition, they do not provide information on the ISM on kpc scales that is typical for extragalactic observations. On the other hand, large-scale galaxy simulations with resolution  $\gtrsim 50$  pc (e.g., Narayanan et al. 2012; Feldmann et al. 2012) cannot resolve the structures of molecular clouds and therefore rely on over-simplified assumptions on the sub-grid gas distribution. Significantly better resolutions have been achieved in isolated Milky Way-like galaxy simulations (e.g., Duarte-Cabral et al. 2015; Richings & Schaye 2016), but they were still insufficient to properly resolve the ISM.

Recently, it has become feasible to simulate a kpc-scale ISM patch and follow star formation and stellar feedback self-consistently, establishing a more realistic, self-regulated system with pc-scale resolution such that the ISM structure and stellar feedback are resolved without resorting to sub-grid models (Gatto et al. 2017; Seifried et al. 2017; Gong et al. 2018; Seifried et al. 2020; Smith et al. 2020). However, most of these studies focus on solar-metallicity, solar-neighborhood conditions, and the only exception (Gong et al. 2020) studied  $X_{\text{CO}}$  with a limited range of  $0.5 \leq Z' \leq 2$ , which still does not cover the “low-metallicity” regime.

In Hu et al. (2021) (hereafter HSvD21), we presented a suite of hydrodynamical simulations of a  $(1 \text{ kpc})^2$  ISM patch with an unprecedented dynamical range spatially and temporally, running for 500 Myr and reaching sub-parsec ( $\sim 0.2$  pc) spatial resolution (which has previously only been achieved with the “zoom-in” techniques and was limited to a few Myrs, e.g., Seifried et al. 2020; Smith et al. 2020). The long simulated time leads to a large sample of clouds at different evolutionary stages, while the sub-parsec resolution is crucial for resolving the compact CO-bright cores at low metallicities. Furthermore, the simulations cover a wide range of metallicities ( $0.1 \leq Z' \leq 3$ ), probing the low-metallicity regime for the first time. The numerical framework self-consistently includes gravity, hydrodynamics, time-dependent cooling and  $\text{H}_2$  chemistry, radiation shielding, individual star formation, and stellar feedback from supernovae and photoionization. To simultaneously resolve the ISM and model the chemistry accurately, a hybrid approach is introduced where  $\text{H}_2$  is followed on-the-fly while the other chemical species, including CO, are modeled in post-processing by a more detailed network.

In this paper, we construct synthetic emission maps of CO(1–0) and CO(2–1) from the simulations in HSvD21 with radiative transfer calculations. Our goal is to investigate the distributions of  $X_{\text{CO}}$  and  $R_{21}$  from pc to kpc scales at different metallicities and how they af-

fect  $X_{\text{CO}}$  and  $R_{21}$  on systematically larger scales. Our paper is organized as follows. Section 2 describes our numerical setup for the radiative transfer calculation on an adaptive mesh. Section 3 is an overview of our simulation results, including our global  $X_{\text{CO}}$  compared against observations. Section 4 is a detailed analysis on the small-scale properties of CO excitation and optical depth. Section 5 shows our predicted  $X_{\text{CO}}$  and  $R_{21}$  on different spatial scales where we systematically increase the beam size from 2 pc to 1 kpc. Section 6 summarizes our work.

## 2. NUMERICAL METHODS

### 2.1. Simulations

Our simulations are presented in detail in HSvD21, which we briefly summarize as follows. The setup is an ISM patch with conditions similar to the solar neighborhood. The box size is 1 kpc along the  $x$ - and  $y$ -axes with periodic boundary conditions and 10 kpc along the  $z$ -axis with outflow boundary conditions. The origin is defined at the box center and  $z = 0$  represents the mid-plane of the disk. The simulations were conducted using the public version of GIZMO (Hopkins 2015), a multi-solver code featuring the meshless Godunov method (Gaburov & Nitadori 2011) built on the TreeSPH code GADGET-3 (Springel 2005). Gravity is solved by the “treecode” method (Barnes & Hut 1986) while hydrodynamics is solved by the meshless finite-mass (MFM) method (Hopkins 2015). Time-dependent cooling and  $\text{H}_2$  chemistry are included based on Glover & Mac Low (2007) and Glover & Clark (2012b), with a HEALPIX (Górski & Hivon 2011)-based treatment for radiation shielding similar to Clark et al. (2012). Star formation is based on the commonly used, stochastic “Schmidt law” recipe with a star formation efficiency of 50%. The stellar masses are stochastically sampled from the stellar initial mass function of Kroupa (2001) which determine the lifetime of massive stars (Ekström et al. 2012) and the luminosity of ionizing radiation (Lejeune et al. 1997, 1998). Supernova feedback is purely thermal. Photoionization follows the method of Hu et al. (2017) that can properly account for overlapping  $\text{H II}$  regions. The far-UV radiation field and cosmic-ray ionization rate are both spatially uniform but time-dependent, scaled linearly with the total star formation rate. The metallicity is assumed to be constant both spatially and temporally.

Four simulations are run with metallicities of  $Z' = 3, 1, 0.3,$  and  $0.1$ . The dust-to-gas mass ratio is 1% at  $Z' = 1$  and scales linearly with  $Z'$ . We first run the  $Z' = 1$  model with an artificially less efficient feedback model for 100 Myr in order to mitigate the initial transient phase that tends to blow out the gaseous disk. This

generates a multiphase ISM structure which is then used by each simulation as the initial conditions. Each simulation is run for 500 Myr. The mass resolution is  $1 M_{\odot}$  per gas particle, which corresponds to  $\sim 0.2$  pc spatial resolution where the Jeans mass is resolved.

The results are further post-processed with a more detailed chemistry network that includes CO chemistry, using the time-dependent  $\text{H}_2$  abundances from the simulations. We assume that an external FUV radiation background (calculated from the SFR) is attenuated by the effects of dust shielding,  $\text{H}_2$  self-shielding, and CO self- and mutual-shielding. The column densities of dust,  $\text{H}_2$ , and CO relevant for shielding are calculated using a pixel-based approach integrated up to a radius of 100 pc for each gas cell. The photodissociation rate coefficients and attenuation coefficients are taken from Heays et al. (2017)<sup>1</sup>. The time-averaged SFR in all runs are close to the observed value in the solar-neighborhood of  $\Sigma_{\text{SFR},0} = 2.4 \times 10^{-3} M_{\odot} \text{ yr}^{-1} \text{ kpc}^{-2}$  (Fuchs et al. 2009) within a factor of 50%. Therefore, the corresponding time-averaged FUV radiation field is close to the Draine field (Draine 1978) and the cosmic-ray ionization rate is close to  $\zeta_{\text{CR}} = 10^{-16} \text{ s}^{-1}$  (Indriolo & McCall 2012; Indriolo et al. 2015) in all runs.

### 2.2. Radiative Transfer on an Adaptive Mesh

We post-process our simulations with the publicly available radiative transfer code RADMC-3D (Dullemond et al. 2012) to generate the synthetic CO(1–0) and CO(2–1) emission maps in the face-on view. We describe the details as follows.

Before we perform radiative transfer, we first need to convert the particle-based gas properties in our simulations onto a mesh where RADMC-3D calculates the level population and the subsequent radiative transfer. Our simulations resolve the Jeans mass of the gas down to  $\sim 0.2$  pc, which defines the smallest spatial scale. However, if we were to generate a uniform Cartesian mesh that covers the entire simulation domain with a spatial resolution of 0.2 pc, it would take  $5000^3$  cells which is computationally infeasible both in terms of computing time and memory. In addition, a large fraction of the simulation domain is filled with CO-free diffuse gas, making a uniform mesh extremely computationally inefficient. As such, it is highly desirable to adopt an adaptive mesh where the finest cells are only employed in regions of dense molecular gas.

We generate an adaptive mesh by first building an octree where each leaf contains at most one gas particle.

<sup>1</sup> <https://home.strw.leidenuniv.nl/~ewine/photo/index.html>



The root node of the octree is centered at  $x = 0.5$  kpc,  $y = 0.5$  kpc, and  $z = 0$ , with a size of 1 kpc on each side, which contains the vast majority of the gas.<sup>2</sup> This octree not only defines an adaptive mesh where the resolution improves (i.e., cell size decreases) with increasing gas density but also serves as a neighbor finder for interpolation (see below). As the smallest physically meaningful scale in our simulations is around 0.2 pc, we trim the mesh such that the size of the smallest cell is  $h_{\text{min}} = 1/2^{13}$  kpc = 0.12 pc (i.e., the maximum refinement level is 13). The mesh is then further refined to fulfill the “2:1 balance,” which avoids a sudden jump of refinement levels and optimizes the calculation of velocity gradients in RADMC-3D.

Once the adaptive mesh is generated, we interpolate the particle information onto the mesh with a scheme similar to the MFM method. For any scalar field  $A$ , the interpolated value at each cell center  $x_c$  is

$$\bar{A}(x_c) = \frac{\sum_j A_j K(|x_j - x_c|, h_j)}{\sum_j K(|x_j - x_c|, h_j)}, \quad (4)$$

where  $x_j$  and  $h_j$  are the location and smoothing length of particle  $j$ , respectively,  $K(|x_j - x_c|, h_j) = \omega(|x_j - x_c|/h_j)/h_j^3$ , and  $\omega$  is the cubic spline kernel function. The summation is over all particles whose kernel overlaps with  $x_c$  (i.e.,  $|x_j - x_c| \leq h_j$ ), which is done by a “scatter”-neighbor search on  $x_c$  using the particle octree. We find that this interpolation scheme is significantly more accurate than the conventional smoothed-particle hydrodynamics (SPH) scheme especially for the gas temperature. The effect of different interpolation schemes is discussed in Appendix D. We interpolate the following quantities onto the adaptive mesh: CO number density ( $n_{\text{CO}}$ ),  $\text{H}_2$  number density ( $n_{\text{H}_2}$ ), gas temperature ( $T$ ), velocity ( $v$ ), and velocity dispersion<sup>3</sup> ( $\sigma_v$ ).

We use the large-velocity gradient approximation module implemented by Shetty et al. (2011a) in RADMC-3D to account for radiation trapping and calculate the level population at each cell. The molecular data are taken from the Leiden Atomic and Molecular database (Schöier et al. 2005). The collision partner of CO is  $\text{H}_2$  with an ortho-to-para ratio of 3, and the collisional rate coefficients are taken from Flower (2001) and Wernli et al. (2006). The local line profile follows a Gaussian function

$$\phi(\nu) = \lambda_0 / (\sqrt{\pi}b) e^{-\Delta\nu^2/b^2}, \quad (5)$$

<sup>2</sup> Gas at high latitude ( $z > 0.5$  kpc) is essentially CO-free and therefore can be excluded without affecting our results.

<sup>3</sup> We first calculate the particle-based  $\sigma_v$  as the velocity dispersion within the gas smoothing length and then interpolate it onto the mesh.

where  $\nu$  is the photon frequency,  $\lambda_0 \equiv c/\nu_0$  ( $c$  is the speed of light and  $\nu_0$  is the line-center photon frequency), and  $\Delta\nu \equiv c(\nu - \nu_0)/\nu_0$  is the Doppler velocity offset. The Doppler parameter  $b \equiv \sqrt{2k_{\text{B}}T/(\mu m_{\text{p}}) + \sigma_v^2}$  accounts for both thermal and microturbulent line broadening, where  $k_{\text{B}}$  is the Boltzmann constant,  $m_{\text{p}}$  is the proton mass, and  $\mu$  is the mean molecular weight.

Once the level populations are known, RADMC-3D solves the equation of radiative transfer along the  $z$ -axis through the adaptive mesh. For each simulation snapshot, we adopt  $512 \times 512$  pixels/rays that cover the entire simulation domain of 1 kpc  $\times$  1 kpc. This means a pixel size of  $1000/512 \approx 2$  pc, which is 16 times coarser than our finest cell. It might therefore seem concerning that a substantial fraction of small cells could be missed by the rays. Fortunately, RADMC-3D has the capability of “recursive sub-pixeling,” where a ray is split into 2-by-2 rays recursively (similar to a quadtree) whenever it passes through a cell smaller than the pixel size. As our pixels coincide with the octree’s hierarchical structure, all cells, including those smaller than 2 pc, are guaranteed to be properly “visited” by the rays and so flux conservation is ensured. This is of crucial importance especially at low metallicities as CO typically concentrates in small dense cores.

At each pixel, RADMC-3D produces a spectrum, i.e., the specific intensity  $I_\nu$  as a function of  $\nu$ . It is convenient to convert  $I_\nu$  into radiation temperature

$$T_{\text{R}} \equiv \frac{\lambda_0^2}{2k_{\text{B}}} I_\nu. \quad (6)$$

The line intensity is defined as the velocity-integrated radiation temperature

$$W \equiv \int T_{\text{R}} dv. \quad (7)$$

which is in units of  $\text{K km s}^{-1}$ . The numerical integration is done with the Simpson’s rule. The velocity coverage of the emission spectra we adopt is  $\pm 20 \text{ km s}^{-1}$ , which is wide enough to cover the vertical motion of the gas. The velocity resolution is  $0.4 \text{ km s}^{-1}$ , which is sufficient considering the thermal broadening alone leads to  $b \approx 1 \text{ km s}^{-1}$  for  $T = 100 \text{ K}$ . An example of typical spectra is shown in Appendix C.

For each snapshot, we run RADMC-3D following the above-mentioned approach and generate  $512 \times 512$  spectra of both the CO(1–0) and CO(2–1) transitions as well as their corresponding maps of line intensity  $W_{10}$  and  $W_{21}$ . We also obtain the number density of CO in the rotational levels  $J = 0, 1$ , and 2 on the adaptive mesh, denoted as  $n_0$ ,  $n_1$ , and  $n_2$ , respectively. We conduct the calculation for 41 snapshots from 100 to 500 Myr with

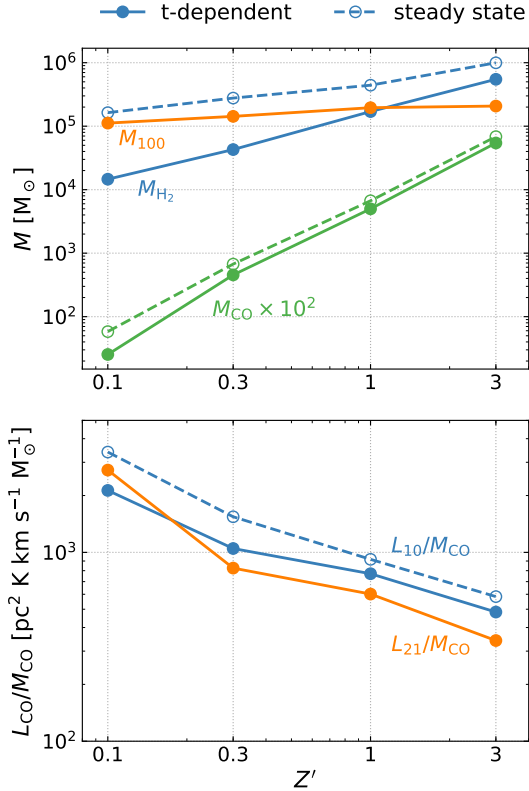


**Figure 2.** *Upper:* Total mass of  $\text{H}_2$  (blue), CO (green, multiplied by 100), and dense gas ( $n > 100 \text{ cm}^{-3}$ , orange) as functions of  $Z'$ . *Lower:* Luminosity-to-mass ratio of CO(1–0) (blue) and CO(2–1) (orange) as functions of  $Z'$ . The time-dependent and steady-state models are shown in solid and dashed lines, respectively.

a time interval of 10 Myr. Throughout the paper, all results we show are time-averaged over 400 Myr, except for the snapshots in Figs. 3 and 4.

### 3. OVERVIEW OF SIMULATION RESULTS

#### 3.1. Global Average Quantities

As shown in HSvD21, due to the long timescale of  $\text{H}_2$  formation on dust grains, the dynamical effect significantly reduces the  $\text{H}_2$  abundances leading to a lower total  $\text{H}_2$  mass ( $M_{\text{H}_2}$ ) in the time-dependent model compared to its steady-state counterpart. In contrast, the effect on the CO abundance and thus the total CO mass ( $M_{\text{CO}}$ ) is much weaker. This is demonstrated in the upper panel of Fig. 2. In addition,  $M_{100}$  represents the total mass of the “dense gas,” which we define as  $n > 100 \text{ cm}^{-3}$ , and it is nearly independent of  $Z'$ , consistent with the fact that the average star formation rate in HSvD21 is insensitive to  $Z'$ . Compared to  $M_{\text{H}_2}$ , the

star formation reservoir transitions from  $\text{H}_2$ -dominated at high  $Z'$  to  $\text{H I}$ -dominated at low  $Z'$ .

While  $M_{\text{H}_2}$ ,  $M_{\text{CO}}$ , and  $M_{100}$  are purely chemical and hydrodynamical properties, the CO luminosity-to-mass ratio ( $L_{\text{CO}}/M_{\text{CO}}$ , lower panel of Fig. 2) is a result of radiative transfer. The luminosities of CO(1–0) and CO(2–1) are defined as  $L_{10} = \int W_{10} da$  and  $L_{21} = \int W_{21} da$ , respectively, where the integration is over the  $(1 \text{ kpc})^2$  area. The luminosity-to-mass ratio is higher at low  $Z'$  mainly because the lines become increasingly optically thin, as will be discussed in Section 4.3.

The time-averaged global conversion factor is  $X_{\text{CO}} = M_{\text{H}_2}/(2m_{\text{p}}L_{10})$  where  $m_{\text{p}}$  is the proton mass. We can now put these computed values in Fig. 1 and compare them against observations. The red filled circles and non-filled triangles represent our time-dependent model and steady-state model, respectively. The red non-filled stars show the “dense gas” conversion factor:  $X_{100} \equiv N_{\text{H}}(n > 100 \text{ cm}^{-3})/W_{10} = 0.71M_{100}/(2m_{\text{p}}L_{10})$ , where the factor 0.71 is the hydrogen mass fraction. Our fiducial time-dependent model can be fitted by (with a correlation coefficient of 0.99):

$$X_{\text{CO}} = 3.17 \times 10^{20} Z'^{-0.71} \text{ cm}^{-2} (\text{K km s}^{-1})^{-1}, \quad (8)$$

which agrees well with the Milky Way value (Eq. (2)) at  $Z' = 1$  within 60%. The metallicity dependence is flatter compared to the steady-state counterpart where  $X_{\text{CO}} \propto Z'^{-1}$ . This is because the dynamical effect mainly suppresses  $\text{H}_2$  formation but not CO formation. The dense gas conversion factor scales even more steeply as  $X_{100} \propto Z'^{-1.5}$ . This demonstrates that the dense, star-forming gas reservoir becomes  $\text{H I}$ -dominated at low  $Z'$ . The implication is that  $X_{\text{CO}}$  at low  $Z'$  can be overestimated both by the spectral synthesis method (by assuming steady-state chemistry) and by the inverse KS method (by assuming the star-forming gas is fully molecular).

At super-solar metallicity ( $Z' = 3$ ), our steady-state model agrees very well with our fiducial time-dependent model. Steady-state chemistry is a good approximation as the  $\text{H}_2$  formation time is short. However, the dense gas conversion factor is significantly lower than  $X_{\text{CO}}$ , which reflects the fact that a large fraction of diffuse (and presumably cold) gas is molecular.

#### 3.2. Visual Impression

Fig. 3 shows face-on maps<sup>4</sup> of  $N_{\text{H}_2}$ ,  $N_{\text{CO}}$ ,  $W_{10}$ , and  $W_{21}$  from left to right with a beam size of  $l_b = 2$  pc in the  $Z' = 1$  run at  $t = 420$  Myr (upper row) and the  $Z' = 0.1$  run at  $t = 130$  Myr (lower row). The entire simulation domain of  $1 \text{ kpc}^2$  is shown. Qualitatively, CO only exists in the inner part of the  $\text{H}_2$  clouds where the gas is dense and well shielded. Both  $\text{H}_2$  and CO are more compact in the  $Z' = 0.1$  case. The distribution of  $W_{10}$  is very similar to that of  $N_{\text{CO}}$  except at the densest cores where  $W_{10}$  is slightly reduced compared to  $N_{\text{CO}}$ . This is because  $\text{CO}(1-0)$  transitions from the optically thin regime where  $W_{10} \propto N_{\text{CO}}$  to the optically thick regime where  $W_{10}$  saturates.  $W_{21}$  follows a similar distribution to  $W_{10}$  but is less spatially extended, as the  $J = 2$  level is not sufficiently excited in the diffuse gas.

However, for extragalactic observations, a pc-scale resolution is often inaccessible. Therefore, we construct  $N_{\text{H}_2}$ ,  $N_{\text{CO}}$ ,  $W_{10}$ , and  $W_{21}$  at coarser beam sizes from our results for  $l_b = 2$  pc. The beam size is systematically increased by factors of two up to  $l_b = 1 \text{ kpc}$ , which includes the entire simulation domain. For example,  $N_{\text{H}_2}$  and  $W_{10}$  at  $l_b = 4$  pc are constructed from the results at  $l_b = 2$  pc:

$$N_{\text{H}_2}(4 \text{ pc}) = \frac{\int N_{\text{H}_2} da}{\int da} = \frac{1}{2^2} \sum_{i=1}^4 N_{\text{H}_2,i}(2 \text{ pc}), \quad (9)$$

$$W_{10}(4 \text{ pc}) = \frac{\int W_{10} da}{\int da} = \frac{1}{2^2} \sum_{i=1}^4 W_{10,i}(2 \text{ pc}), \quad (10)$$

where the integration is over the area of a 4 pc beam and the summation is over the 2-by-2 sub-beams of  $l_b = 2$  pc which constitute a 4 pc beam. Likewise, a 8 pc beam is constructed from the 4-by-4 sub-beams of 2 pc (or, equivalently, from the 2-by-2 sub-beams of 4 pc), and so forth.

To illustrate the effect of spatial averaging/smoothing, Fig. 4 shows the maps of  $W_{10}$  (upper row) and  $X_{\text{CO}}$  (lower row) for  $l_b = 2, 8, 32, 125,$  and  $500$  pc from left to right. On 2 pc scale,  $X_{\text{CO}}$  varies by orders of magnitude: it is low in the dense, well-shielded gas and high in the diffuse gas. We stress that our radiative transfer calculations are done with a much smaller minimal cell size  $\sim 0.2$  pc with the sub-pixeling technique (see Section 2.2). On large scales, as long as the beam contains dense gas (which only occupies a small area), the beam-averaged  $X_{\text{CO}}$  is driven towards low values (in purple). This will be discussed more quantitatively in Section 5

<sup>4</sup> We note that HsvD21 distinguishes between the line-of-sight integrated column density ( $N^{\text{obs}}$ ) and the column density available for radiation shielding ( $N^{\text{eff}}$ ). In this work, we refer by column density exclusively to  $N^{\text{obs}}$ .

after we provide more insight and background information on the simulations at the molecular level in Section 4.

### 3.3. Chemical Properties

In this section, we briefly describe the distributions of  $\text{H}_2$  and CO in the simulations. Although these chemical properties have been shown in HsvD21, they are the basis of our radiative transfer and provide context for the results in Fig. 4, so they are worth repeating here.

We define the number abundance of a chemical species  $i$  as  $x_i \equiv n_i/n$ , where  $n$  is the hydrogen number density and  $n_i$  is the number density of species  $i$ . The normalized fractional abundance of  $\text{H}_2$  is then defined as  $f_{\text{H}_2} \equiv 2x_{\text{H}_2}$  such that  $f_{\text{H}_2} = 1$  when all hydrogen is in the form of  $\text{H}_2$ . Similarly, the normalized fractional abundance of CO is defined as  $f_{\text{CO}} \equiv x_{\text{CO}}/x_{\text{C},0}$ , where  $x_{\text{C},0} = 1.4 \times 10^{-4} Z'$  is the total carbon abundance. The left panel of Fig. 5, shows  $f_{\text{H}_2}$  (solid lines) and  $f_{\text{CO}}$  (dashed lines) as functions  $n$ . At a given  $Z'$ , CO forms at higher densities than where  $\text{H}_2$  forms, consistent with the visual impression in Fig. 3. Both  $\text{H}_2$  and CO exist at increasingly higher densities as  $Z'$  decreases due to the deficit of dust.

The right panel of Fig. 5 shows  $N_{\text{CO}}$  as a function of  $N_{\text{H}_2}$ . The  $N_{\text{H}_2} - N_{\text{CO}}$  relation is characterized by three regimes: (i) The CO-poor regime at low  $N_{\text{H}_2}$  where the CO-to- $\text{H}_2$  ratio  $\gamma \equiv N_{\text{CO}}/N_{\text{H}_2}$  is low; (ii) the transition regime at intermediate  $N_{\text{H}_2}$  where  $\gamma$  increases sharply with  $N_{\text{H}_2}$  which reflects the formation of CO; and (iii) the CO-rich regime at high  $N_{\text{H}_2}$  where  $\gamma$  approaches its upper limit (indicated by the thin dashed lines).

## 4. MOLECULAR PHYSICS

In this section, we present a detailed analysis of the “microphysics” in our simulations and discuss how the lines are excited and propagated in the ISM, which forms the backbone of the observables. The readers interested only in our predicted  $X_{\text{CO}}$  and  $R_{21}$  may want to skip this section and go directly to Section 5.

### 4.1. CO Excitation

In the upper panel of Fig. 6, we show the excitation temperature of  $\text{CO}(1-0)$  ( $T_{\text{exc}}$ , solid lines) and kinetic temperature ( $T_{\text{kin}}$ , dashed lines) as a function of  $n$ . In low-density gas where collisions are unimportant,  $T_{\text{exc}}$  is set by the background radiation  $T_{\text{bg}} = 2.73$  K due to the cosmic microwave background (CMB). As  $n$  increases,  $T_{\text{exc}}$  gradually increases and approaches  $T_{\text{kin}}$ , and the line is “thermalized” when  $T_{\text{exc}} = T_{\text{kin}}$ . At the highest densities,  $T_{\text{kin}}$  (and therefore  $T_{\text{exc}}$ ) is higher at

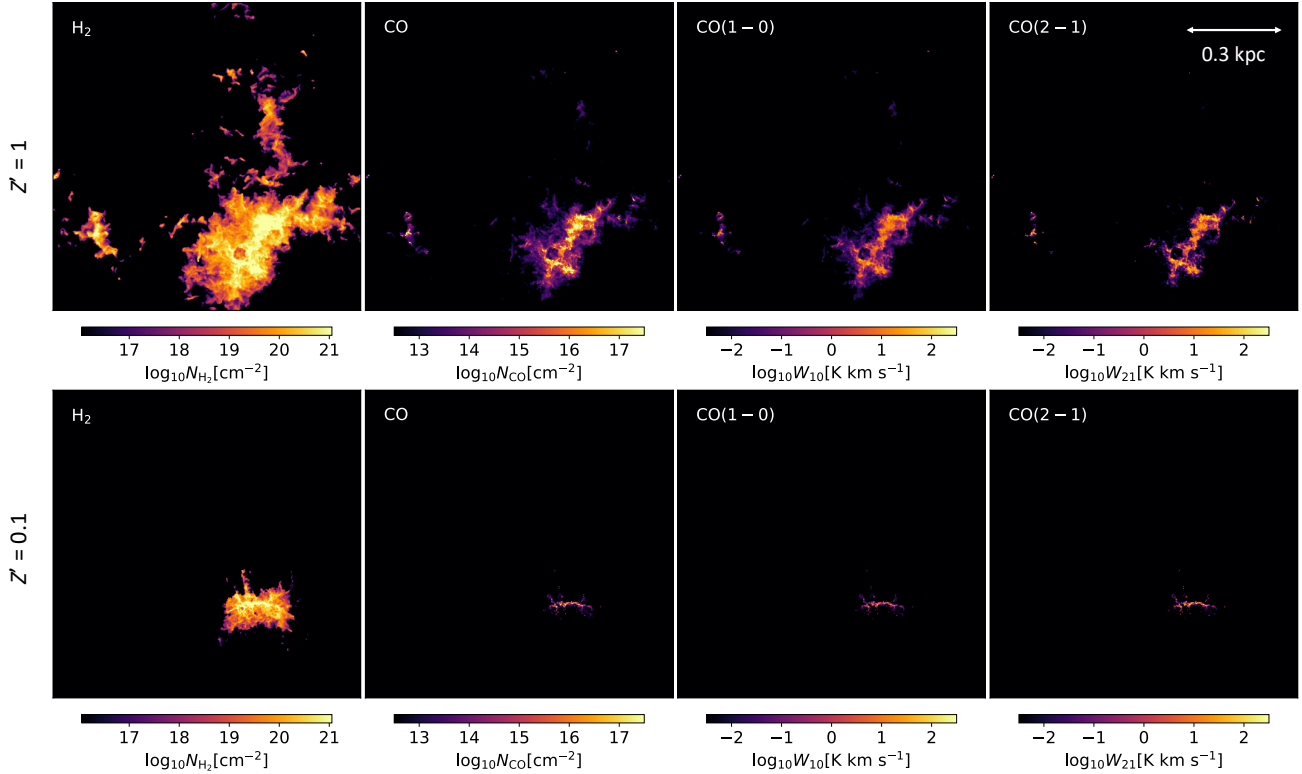


**Figure 3.** Face-on maps of  $\text{H}_2$  column density, CO column density, CO(1–0) line intensity, and CO(2–1) line intensity from left to right in the solar metallicity ( $Z' = 1$ ) run at  $t = 420$  Myr (upper row) and the  $Z' = 0.1$  run at  $t = 130$  Myr (lower row). The entire simulation domain of  $1 \text{ kpc}^2$  is shown.  $\text{H}_2$  is spatially more extended than CO. Both  $\text{H}_2$  and CO are more compact at low metallicity.

low  $Z'$  due to heating from  $\text{H}_2$  formation and UV pumping (Bialy & Sternberg 2019). Interestingly, CO(1–0) is thermalized at higher densities as  $Z'$  decreases. This is caused by a combination of two effects at low  $Z'$ . Firstly, the collision partner  $\text{H}_2$  forms at densities higher than the critical density of CO(1–0). Therefore, it takes a higher total hydrogen number density to thermalize the line. Secondly, higher CO abundance results in more efficient radiation trapping (more optically thick) and thus a lower effective critical density.

The CO population ratio ( $r_{21}$ ) of level  $J = 2$  to level  $J = 1$  follows a similar trend. In the lower panels of Fig. 6, we show  $r_{21}$  as a function of  $n$  (left) and  $n_{\text{H}_2}$  (right) in solid lines. Analytically, the population ratio of level  $J$  to level  $J' = J - 1$  can be expressed as a function of  $T_{\text{exc}}$ :

$$\begin{aligned} r_{JJ'}(T_{\text{exc}}) &= \frac{(2J+1)e^{-B_0 J(J+1)/T_{\text{exc}}}}{(2J'+1)e^{-B_0 J'(J'+1)/T_{\text{exc}}}} \\ &= \frac{g_J}{g_{J'}} e^{-T_{JJ'}/T_{\text{exc}}}, \end{aligned} \quad (11)$$

where  $g_J$  and  $g_{J'}$  are the degeneracy in level  $J$  and  $J'$ , respectively,  $B_0 = 2.77 \text{ K}$ ,  $T_{JJ'} = 2JB_0 = E_{JJ'}/k_B$ , and  $E_{JJ'}$  is the energy difference between levels  $J$  and

$J'$ . For  $J = 2$  and  $J' = 1$ , it follows

$$r_{21}(T_{\text{exc}}) = \frac{5}{3} e^{-11.1 \text{ K}/T_{\text{exc}}}. \quad (12)$$

Note that  $T_{\text{exc}}$  here is specifically for CO(2–1) which can be different from the excitation temperature of CO(1–0) unless the gas is in LTE. At low densities where  $T_{\text{exc}} = 2.73 \text{ K}$ , our results agree well with the analytic expectation  $r_{21}(2.73 \text{ K}) = 0.029$ . As  $n$  increases,  $r_{21}$  gradually increases and approaches the LTE line ratio  $r_{21,\text{LTE}}$  (dashed lines), which we obtain using Eq. (12) assuming  $T_{\text{exc}} = T_{\text{kin}}$ . At  $Z' \geq 1$ , the decline of  $r_{21}$  at high  $n$  is due to the decline of  $T_{\text{kin}}$  instead of sub-thermal excitation. The maximum  $r_{21}$  is around unity at all metallicities and is slightly higher at low  $Z'$  due to higher  $T_{\text{kin}}$ , though the effect is very mild. Indeed, Eq. (12) suggests that  $r_{21}$  is not very sensitive to  $T_{\text{exc}}$  when  $T_{\text{exc}} \gg 11.1 \text{ K}$  and it asymptotes to an upper limit of  $5/3 \approx 1.66$  as  $T_{\text{exc}} \rightarrow \infty$ .

#### 4.2. Optically Thin Limit

At low  $N_{\text{CO}}$ , the lines are in the optically thin limit and self-absorption can be neglected. The emissivity of



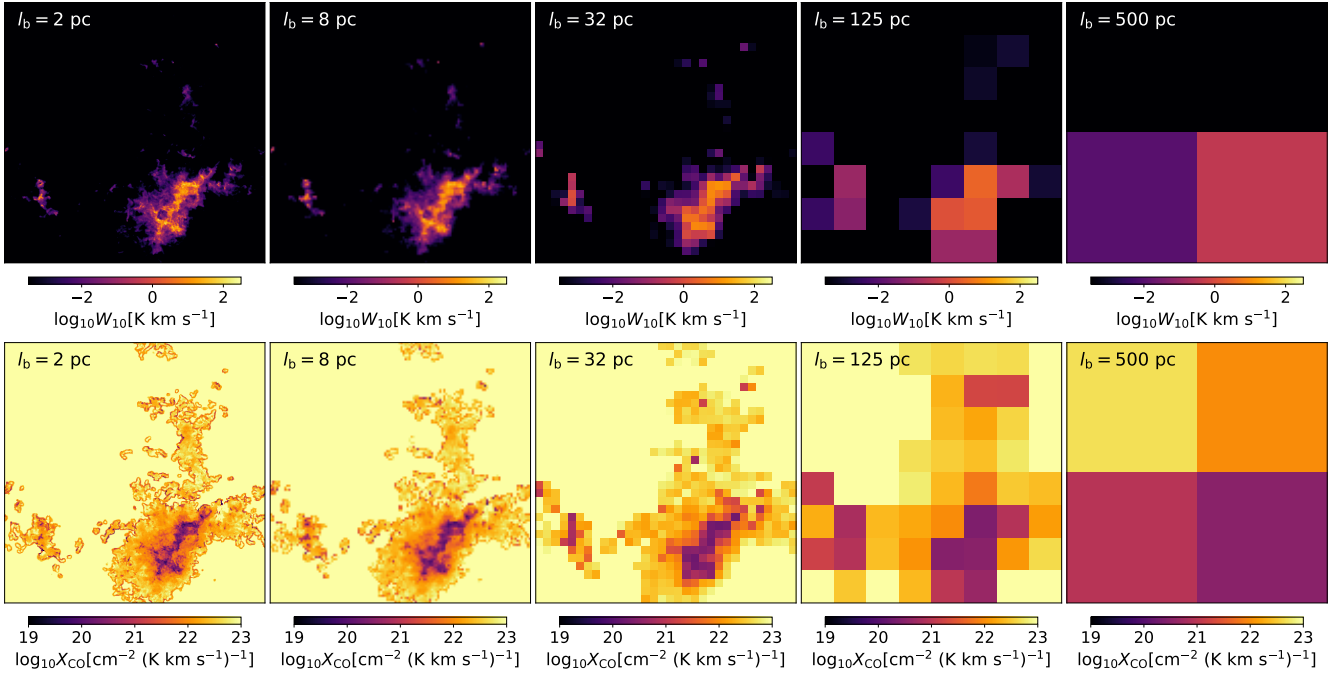


**Figure 4.** Face-on maps of  $W_{10}$  (upper row) and  $X_{\text{CO}}$  (lower row) with beam size  $l_b = 2, 8, 32, 125,$  and  $500$  pc from left to right. Note that the Milky Way  $X_{\text{CO}}$  factor (Eq. (2)) is represented by the dark purple color.

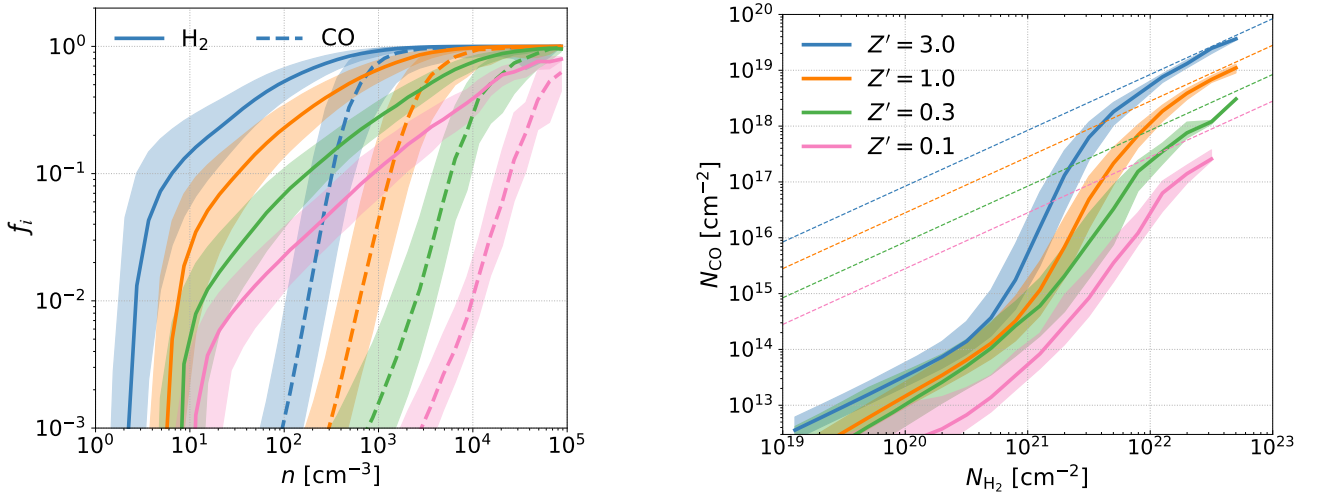


**Figure 5.** *Left:* Normalized fractional abundance of  $\text{H}_2$  (solid lines) and  $\text{CO}$  (dashed lines) as functions of hydrogen number density  $n$  for normalized metallicity  $Z' = 3, 1, 0.3,$  and  $0.1$ . *Right:*  $\text{H}_2$  column density vs.  $\text{CO}$  column density for  $Z' = 3, 1, 0.3,$  and  $0.1$ . The thin dashed lines indicate the maximum ratio  $N_{\text{CO}}/N_{\text{H}_2} = 2x_{\text{C},0}$  where carbon is completely in form of  $\text{CO}$ . In both panels, the lines represent the median values while the shaded areas enclose the 25th and 75th percentiles.

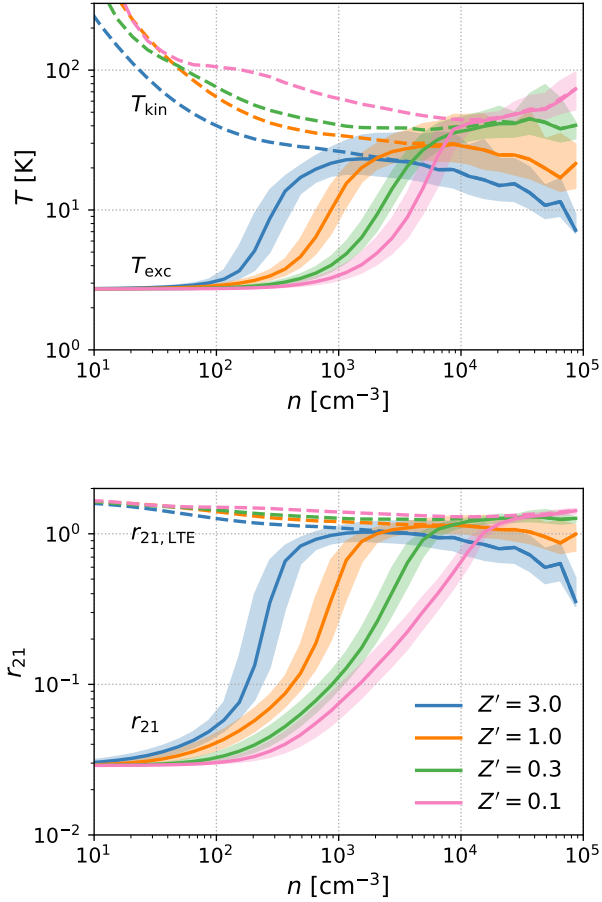


**Figure 6.** *Upper panel:* Excitation temperature of CO(1–0) ( $T_{\text{exc}}$ , solid lines) and kinetic temperature ( $T_{\text{kin}}$ , dashed lines) as a function of  $n$ . *Lower panel:* CO population ratio of  $J = 2$  to  $J = 1$  ( $r_{21}$ , solid lines) as a function of  $n$ . The dashed lines show the CO population ratio assuming local thermodynamic equilibrium ( $r_{21,\text{LTE}}$ ). The lines represent the median values while the shaded areas enclose the 25th and 75th percentiles (not shown for  $T_{\text{kin}}$  and  $r_{21,\text{LTE}}$  for the sake of clarity). The lines thermalize at higher densities at low  $Z'$  as the collision partner  $\text{H}_2$  forms at densities higher than the critical densities and the lower CO abundance leads to less efficient radiation trapping.

the CO( $J-J'$ ) transition is

$$j_\nu = \frac{E_{JJ'}}{4\pi} n_J A_{JJ'} \phi(\nu), \quad (13)$$

where  $n_J$  is the number density of CO in level  $J$  and  $A_{JJ'}$  is the Einstein coefficient for spontaneous decay. As there is no absorption, the specific intensity is simply  $I_\nu = \int j_\nu dz$  and thus the line intensity can be written as

$$\begin{aligned} W_{JJ',\text{thin}} &= \frac{\lambda_{JJ'}^2}{2k_B} \iint j_\nu dz dv \\ &= \frac{\lambda_{JJ'}^3}{8\pi} T_{JJ'} A_{JJ'} \int n_{\text{CO}} f_J dz, \end{aligned} \quad (14)$$

where  $\lambda_{JJ'} = hc/E_{JJ'}$  is the line-center wavelength,  $h$  is the Planck constant, and  $f_J \equiv n_J/n_{\text{CO}}$  is the fraction of CO in level  $J$ . If we define the  $n_{\text{CO}}$ -weighted line-of-sight (l.o.s.) average  $\bar{f}_J$  as

$$\bar{f}_J \equiv \frac{\int n_{\text{CO}} f_J dz}{\int n_{\text{CO}} dz} = \frac{N_{\text{CO},J}}{N_{\text{CO}}}, \quad (15)$$

where  $N_{\text{CO}}$  is the CO column density and  $N_{\text{CO},J}$  is the column density of CO in level  $J$ , we obtain

$$W_{JJ',\text{thin}} = \frac{\lambda_{JJ'}^3}{8\pi} T_{JJ'} A_{JJ'} N_{\text{CO}} \bar{f}_J. \quad (16)$$

Namely,  $W_{JJ',\text{thin}}$  scales linearly with  $N_{\text{CO}}$ , with a secondary dependency on  $\bar{f}_J$ . Note that Eq. (16) is independent of the line width  $b$  as expected for optically thin conditions.

Analytically,  $f_J$  can be expressed as a function of the excitation temperature  $T_{\text{exc}}$

$$\begin{aligned} f_J(T_{\text{exc}}) &= \frac{(2J+1)e^{-B_0 J(J+1)/T_{\text{exc}}}}{\sum_J (2J+1)e^{-B_0 J(J+1)/T_{\text{exc}}}} \\ &\approx \frac{(2J+1)e^{-B_0 J(J+1)/T_{\text{exc}}}}{\sqrt{1 + (T_{\text{exc}}/B_0)^2}}, \end{aligned} \quad (17)$$

where the approximation of the partition function in the denominator is accurate to within  $\pm 6\%$  for all  $T_{\text{exc}}$  (Draine 2011, ch. 19). Adopting  $A_{10} = 7.2 \times 10^{-8} \text{ s}^{-1}$ ,  $A_{21} = 6.91 \times 10^{-7} \text{ s}^{-1}$ ,  $T_{10} = 5.53 \text{ K}$ ,  $T_{21} = 11.1 \text{ K}$ ,  $\lambda_{10} = 0.26 \text{ cm}$ , and  $\lambda_{21} = 0.13 \text{ cm}$ , the line intensities in the optically thin regime become

$$W_{10,\text{thin}} = 7.82 \text{ K km s}^{-1} N_{\text{CO},16} \frac{\bar{f}_1}{f_1(2.73)}, \quad (18)$$

$$W_{21,\text{thin}} = 0.54 \text{ K km s}^{-1} N_{\text{CO},16} \frac{\bar{f}_2}{f_2(2.73)}, \quad (19)$$

where  $N_{\text{CO},16} \equiv N_{\text{CO}}/(10^{16} \text{ cm}^{-2})$ .

In the left panels in Fig. 7, we show  $W_{10}$  (upper) and  $W_{21}$  (lower) as functions of  $N_{\text{CO}}$  at different  $Z'$ . At the lowest  $N_{\text{CO}}$  where collisional excitation is inefficient,  $T_{\text{exc}} = 2.73 \text{ K}$  and thus  $W_{10}$  and  $W_{21}$  follow the dashed lines which indicate  $W_{10} = 7.82 N_{\text{CO},16} \text{ K km s}^{-1}$  and  $W_{21} = 0.54 N_{\text{CO},16} \text{ K km s}^{-1}$  in the upper and lower panels, respectively. For  $N_{\text{CO}} < 10^{16} \text{ cm}^{-2}$ ,  $W_{10}$  scales linearly with  $N_{\text{CO}}$  as the secondary factor  $\bar{f}_1$  does not vary much with  $N_{\text{CO}}$ . This is shown in the upper right panel of Fig. 7. Since the  $J = 1$  level is only 5.53 K above the ground state, it is already significantly excited by the CMB radiation alone ( $f_1(2.73 \text{ K}) = 0.28$ ). In contrast,  $W_{21}$  scales super-linearly with  $N_{\text{CO}}$  in the optically thin regime where  $\bar{f}_2$  provides a secondary contribution. Indeed,  $\bar{f}_2$  increases significantly with  $N_{\text{CO}}$ ,

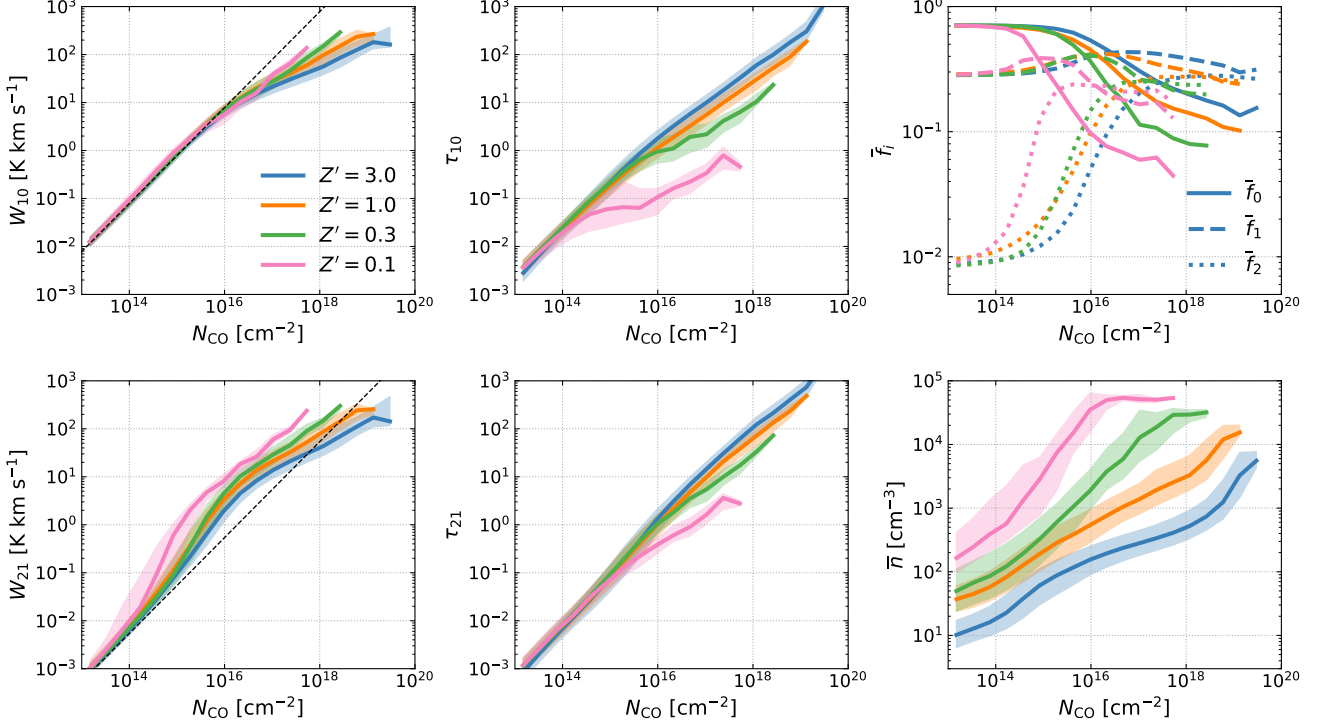


**Figure 7.** *Left:* Line intensity of CO(1–0) (upper) and CO(2–1) (lower) as a function of  $N_{\text{CO}}$ . The dashed lines in the upper and lower panels indicate  $W_{10,\text{thin}}/N_{\text{CO},16} = 7.82$  K km s<sup>-1</sup> and  $W_{21,\text{thin}}/N_{\text{CO},16} = 0.54$  K km s<sup>-1</sup>, respectively. *Middle:* Optical depth of CO(1–0) (upper) and CO(2–1) (lower) as a function of  $N_{\text{CO}}$ . *Upper right:* The  $n_{\text{CO}}$ -weighted average fraction of CO in the rotational level  $J = 0$  (solid), 1 (dashed), and 2 (dotted) as functions of  $N_{\text{CO}}$ . *Lower right:* The  $n_{\text{CO}}$ -weighted average hydrogen number density as a function of  $N_{\text{CO}}$ . The lines represent the median values while the shaded areas enclose the 25th and 75th percentiles in all panels (not shown for  $\bar{f}_J$  for the sake of clarity).

from  $f_2$  (2.73 K) =  $8.08 \times 10^{-3}$  to a maximum value of  $\sim 0.3$ .

In addition, the excitation of both  $J = 1$  and  $J = 2$  occurs at lower  $N_{\text{CO}}$  as  $Z'$  decreases. Assuming a positive correlation between  $n$  and  $N_{\text{CO}}$ , this seems to be in conflict with Fig. 6 where thermalization occurs at higher densities at low  $Z'$ . However, since CO only exists in the small and dense cores at low  $Z'$ , the corresponding gas density is higher at a given  $N_{\text{CO}}$ . This is demonstrated in the lower right panel of Fig. 7, where we show the  $n_{\text{CO}}$ -weighted l.o.s. average hydrogen number density,

$$\bar{n} \equiv \frac{\int n_{\text{CO}} n \, dz}{\int n_{\text{CO}} \, dz}, \quad (20)$$

as a function of  $N_{\text{CO}}$ . Indeed,  $\bar{n}$  correlates positively with  $N_{\text{CO}}$  at all  $Z'$ . However, at a given  $N_{\text{CO}}$ ,  $\bar{n}$  increases inversely with  $Z'$ . The net effect is that as  $Z'$  decreases the excitation of both  $J = 1$  and  $J = 2$  occurs at a lower  $N_{\text{CO}}$ .

#### 4.3. Optical Depth Effect

The optical depth at the line center of CO( $J$ – $J'$ ) can be expressed as

$$\tau_{JJ'} = \frac{\lambda_{JJ'}^3 A_{JJ'} g_J}{8\pi^{3/2} g_{J'}} \int \frac{n_{J'}}{b} \left( 1 - \frac{n_J g_{J'}}{n_{J'} g_J} \right) dz. \quad (21)$$

Adopting  $g_0 = 1$ ,  $g_1 = 3$ , and  $g_2 = 5$ , we obtain

$$\tau_{10} = 8.53 N_{\text{CO},16} \frac{\bar{f}_0}{b_5} \left( 1 - \frac{r_{10}}{3} \right) \quad (22)$$

and

$$\tau_{21} = 5.68 N_{\text{CO},16} \frac{\bar{f}_1}{b_5} \left( 1 - \frac{3r_{21}}{5} \right), \quad (23)$$

where  $b_5 \equiv b/(10^5 \text{ cm s}^{-1})$ . We numerically calculate the  $n_{\text{CO}}$ -weighted l.o.s. average terms in Eqs. (22) and (23) and show them as functions of  $N_{\text{CO}}$  in the middle panels of Fig. 7.

Adopting characteristic values  $b_5 = 2$  and  $T_{\text{exc}} = 10$  K, we expect  $\tau_{10} = 1$  at  $N_{\text{CO}} \sim 2.1 \times 10^{16} \text{ cm}^{-2}$  and  $\tau_{21} = 1$  at  $N_{\text{CO}} \sim 1.2 \times 10^{16} \text{ cm}^{-2}$ , respectively. This analytic estimate agrees well with our results (except for the  $Z' = 0.1$  case where the  $T_{\text{exc}}$  is much higher). At

higher  $N_{\text{CO}}$ , the lines become optically thick and thus both  $W_{10}$  and  $W_{21}$  start to flatten and scale sub-linearly with  $N_{\text{CO}}$ .

At a given  $N_{\text{CO}}$ ,  $\tau_{10}$  decreases with  $Z'$ . This is caused by the corresponding higher density ( $\bar{n}$ ) that more efficiently excites the upper level  $J = 1$ , which means (i) higher  $r_{10}$  and thus more efficient stimulated emission and (ii) lower  $f_0$  as the ground level  $J = 0$  is depopulated. In other words, CO(1–0) becomes increasingly optically thin as  $Z'$  decreases. In particular, at  $Z' = 0.1$ ,  $\tau_{10}$  never exceeds unity at all  $N_{\text{CO}}$ . On the other hand,  $\tau_{21}$  shows a similar dependency on  $Z'$ , but the effect is less significant than for  $\tau_{10}$ , as  $f_1$  does not vary with  $N_{\text{CO}}$  as much as  $f_0$ . Therefore, at  $Z' = 0.1$ ,  $\tau_{21}$  does eventually become optically thick, reaching a maximum of three at the highest  $N_{\text{CO}}$ .

Observationally, the excitation temperature of CO(1–0) can be estimated from the peak of the observed radiation temperature  $T_{\text{R,max}}$  (e.g., Pineda et al. 2008). This is based on the radiative transfer equation in a uniform medium:

$$T_{\text{R}} = T_{10} \left( \frac{1}{e^{T_{10}/T_{\text{exc}}} - 1} - \frac{1}{e^{T_{10}/T_{\text{bg}}} - 1} \right) (1 - e^{-\tau}). \quad (24)$$

If the line is sufficiently optically thick ( $\tau \gg 1$ ), the excitation temperature can be expressed as

$$T_{\text{exc,s}} = \frac{T_{10}}{\ln \left( 1 + T_{10} / \left( T_{\text{R,max}} + \frac{T_{10}}{e^{T_{10}/T_{\text{bg}}} - 1} \right) \right)}. \quad (25)$$

In reality, however, molecular clouds are highly inhomogeneous. As long as the line is optically thick, one can only observe emission that originates from the cloud surface up to a thickness of  $\tau \approx 1$  where the density is lower and thus  $T_{\text{exc}}$  is lower. Therefore, Eq. (25) only measures the excitation temperature at the cloud surface (and hence the subscript “s”). In the upper panels of Fig. 8, the blue solid lines show  $T_{\text{exc,s}}$  as a function of  $N_{\text{CO}}$  for  $Z' = 3, 1, 0.3$ , and  $0.1$  from left to right. Note that we only show  $T_{\text{exc,s}}$  in the optically thick regime ( $\tau_{10} > 1$ ) where Eq. (25) is applicable. At  $Z' = 0.1$ ,  $\tau_{10} < 1$  everywhere and thus  $T_{\text{exc,s}}$  is not shown. Comparing with the  $n_{\text{CO}}$ -weighted l.o.s. average excitation temperature:

$$\bar{T}_{\text{exc}} \equiv \frac{\int n_{\text{CO}} T_{\text{exc}} dz}{\int n_{\text{CO}} dz}, \quad (26)$$

as shown by the orange dashed lines, we see that  $T_{\text{exc,s}}$  is indeed slightly lower than  $\bar{T}_{\text{exc}}$  though the effect is mild (less than a factor of two). Finally, the green dotted lines are the  $n_{\text{CO}}$ -weighted l.o.s. average kinetic temperature:

$$\bar{T}_{\text{kin}} \equiv \frac{\int n_{\text{CO}} T_{\text{kin}} dz}{\int n_{\text{CO}} dz}. \quad (27)$$

$\bar{T}_{\text{exc}}$  gradually increases and approaches  $\bar{T}_{\text{kin}}$  as  $N_{\text{CO}}$  increases. Note that  $\bar{T}_{\text{exc}} < \bar{T}_{\text{kin}}$  at almost all  $N_{\text{CO}}$ . Therefore, the fact that  $\bar{T}_{\text{exc}}$  (and thus  $T_{\text{exc,s}}$ ) increases with  $N_{\text{CO}}$  is mainly driven by the increase of average density instead of a temperature effect as  $\bar{T}_{\text{kin}}$  is nearly constant. This also explains why  $W_{10}$  does not scale as  $\ln(N_{\text{CO}})$  in the optically thick regime ( $N_{\text{CO}} \gtrsim 10^{16} \text{ cm}^{-2}$ ), as the theory of curve of growth would predict. Instead,  $W_{10}$  increases more rapidly with  $N_{\text{CO}}$  (see Fig. 7), as  $T_{\text{exc,s}}$  provides an extra contribution to the growth of  $W_{10}$ .

Similarly, the lower panels of Fig. 8 show the line ratio ( $R_{21}$ ) in blue solid lines as a function of  $N_{\text{CO}}$  for  $Z' = 3, 1, 0.3$ , and  $0.1$  from left to right. The “optically thin” line ratio

$$R_{21,\text{thin}} \equiv \frac{W_{21,\text{thin}}}{W_{10,\text{thin}}} = 2.4 \frac{\bar{f}_2}{f_1} \quad (28)$$

(from Eqs. (18) and (19)) is shown by orange dashed lines while the “LTE optically thin” line ratio

$$R_{21,\text{LTE}}(T_{\text{kin}}) \equiv 2.4 \frac{\bar{f}_2(T_{\text{kin}})}{f_1(T_{\text{kin}})} \quad (29)$$

is shown by green dotted lines.

In the optically thin regime,  $R_{21} = R_{21,\text{thin}}$  by definition. At the lowest  $N_{\text{CO}}$ , the excitation is set by the CMB temperature and therefore  $R_{21} = R_{21,\text{thin}} = 2.4 f_2(2.73)/f_1(2.73) = 0.069$ . As  $N_{\text{CO}}$  increases, the average density also increases which gradually drives  $R_{21,\text{thin}}$  towards  $R_{21,\text{LTE}}$ , similar to the behavior of  $r_{21}$  shown in Fig. 6. The maximum of  $R_{21,\text{thin}}$  is  $\sim 2.5$  and is insensitive to  $Z'$  (as is the case for  $r_{21}$ ). Note that the maximum theoretical line ratio is  $R_{21,\text{LTE}}(\infty) = 4$ . In addition, at lower  $Z'$ ,  $R_{21}$  rises up at a lower  $N_{\text{CO}}$  because of the density effect as shown in Fig. 7. At high  $N_{\text{CO}}$ ,  $R_{21}$  falls slightly below  $R_{21,\text{thin}}$  by about a factor of two due to the optical depth effect: as both lines become optically thick, the observed  $R_{21}$  originates from the cloud surfaces with thickness of  $\tau \approx 1$ , where the density is lower and the level population is more subthermal. However, at  $Z' = 0.1$ , both lines are only marginally optically thick and thus  $R_{21}$  becomes closer to its optically thin limit  $R_{21,\text{thin}}$ , reaching a maximum of  $\sim 1.5$ , (about 50% larger than the higher  $Z'$  cases).

## 5. OBSERVATIONAL IMPLICATIONS

### 5.1. Spatially Resolved $X_{\text{CO}}$ and $R_{21}$

Armed with the detailed background in Section 4, we are now in a good position to study the small-scale distributions of  $X_{\text{CO}}$  and  $R_{21}$ . The left panel of Fig. 9 shows  $W_{10}$  as a function of  $N_{\text{H}_2}$  at different

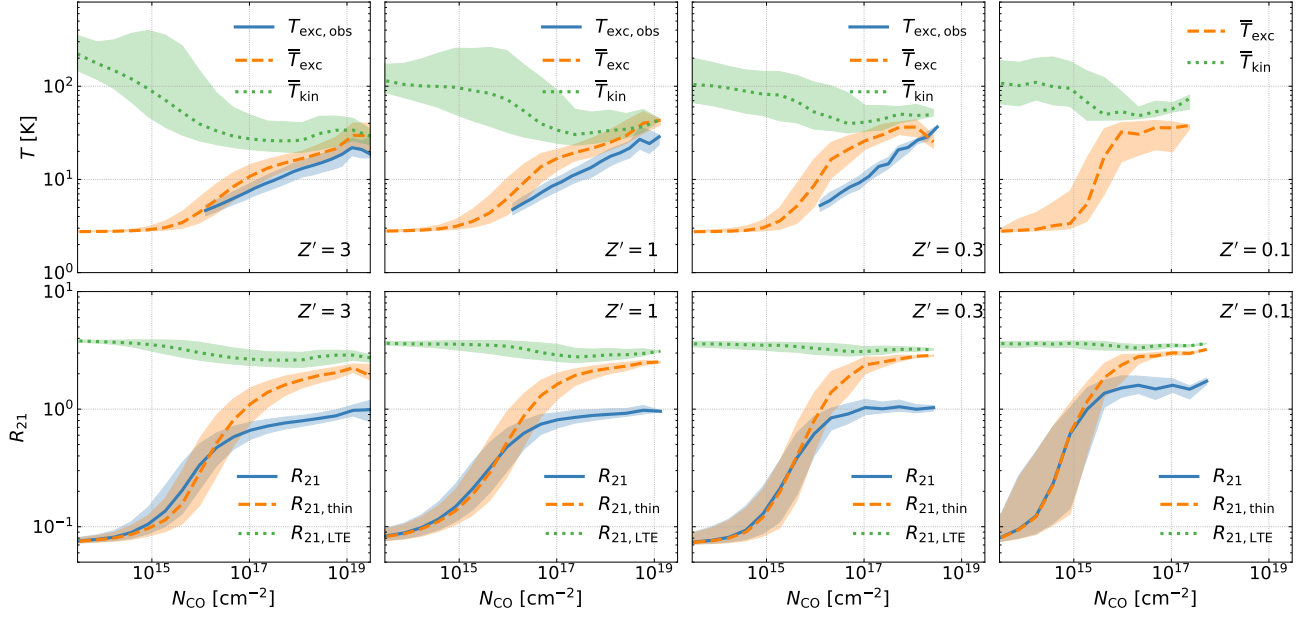


**Figure 8.** *Upper panels:* Cloud surface excitation temperature as would be observed (blue solid, see Eq. (25)), CO density-weighted average excitation temperature (orange dashed, see Eq. (26)), and CO density-weighted average kinetic temperature (green dotted, see Eq. (27)) as functions of  $N_{\text{CO}}$  for  $Z' = 3, 1, 0.3,$  and  $0.1$  from left to right. *Lower panels:* Observed line ratio  $R_{21} \equiv W_{21}/W_{10}$  (blue solid), “optically thin” line ratio (orange dashed, see Eq. (28)), and “optically thin” line ratio assuming LTE (green dotted, see Eq. (29)) as functions of  $N_{\text{CO}}$  for  $Z' = 3, 1, 0.3,$  and  $0.1$  from left to right. The lines represent the median values while the shaded areas enclose the 25th and 75th percentiles in all panels. The observed excitation temperature and line ratio are slightly lower than the l.o.s. averages as only the cloud surfaces can be seen for optically thick lines.

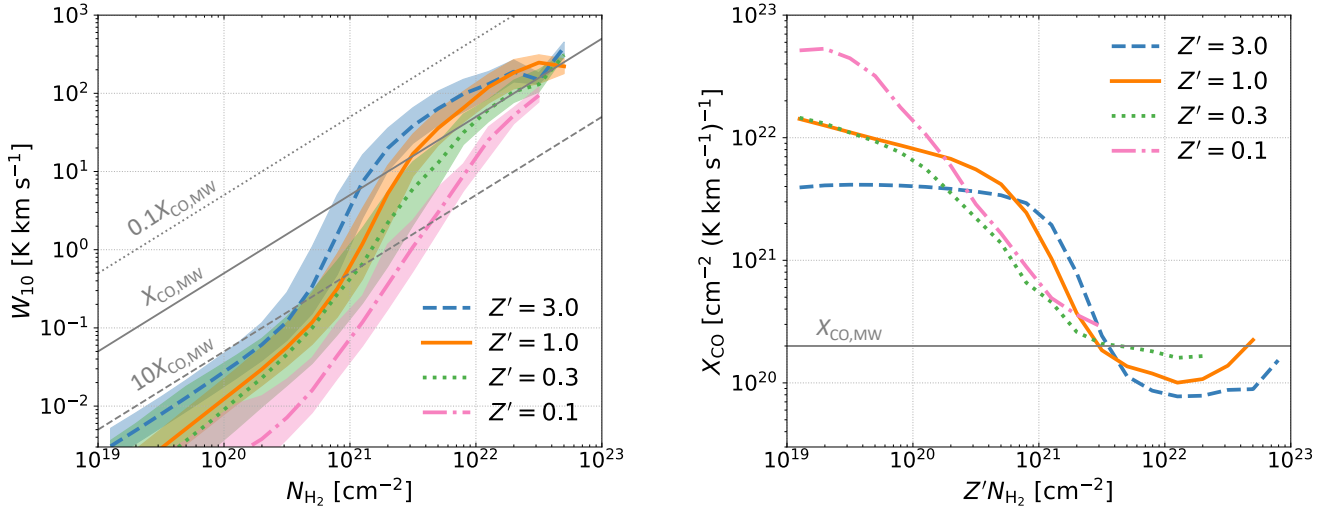


**Figure 9.** *Left:* CO(1-0) line intensity as a function of H $_2$  column density ( $N_{\text{H}_2}$ ). The lines represent the median values while the shaded areas enclose the 25th and 75th percentiles. The dotted, solid, and dashed lines in grey indicate  $X_{\text{CO}}/X_{\text{CO, MW}} = 0.1, 1,$  and  $10,$  respectively. The variation of  $X_{\text{CO}}$  is mainly driven by the variation of CO abundance. *Right:*  $X_{\text{CO}}$  as a function of  $Z' N_{\text{H}_2}$ . The scatter is not shown for clarity.  $X_{\text{CO}}$  drops to the Milky Way value ( $X_{\text{CO, MW}}$ , horizontal grey line) at  $Z' N_{\text{H}_2} \sim 3 \times 10^{21}$  cm $^{-2}$  (visual extinction  $A_V \sim 3$ ) where dust shielding becomes effective.



$Z'$ . The dotted, solid, and dashed lines in grey indicate  $X_{\text{CO}}/X_{\text{CO,MW}} = 0.1, 1, \text{ and } 10$ , respectively. Recall from Fig. 7 that  $W_{10} < 10 \text{ K km s}^{-1}$  (or  $N_{\text{CO}} < 10^{16} \text{ cm}^{-3}$ ) is the optically thin regime where  $W_{10} \propto N_{\text{CO}}$ . It is also in this regime that  $X_{\text{CO}}$  varies the most, which corresponds to the formation of CO (see Fig. 5). At  $W_{10} > 10 \text{ K km s}^{-1}$ , the line becomes optically thick and  $W_{10}$  flattens, except for the  $Z' = 0.1$  case where the line remains optically thin. In this optically thick regime,  $X_{\text{CO}}$  only varies mildly. Therefore, the variation of  $X_{\text{CO}}$  mostly occurs in the optically thin regime and is driven by the variation of CO abundance. Note that even at  $Z' = 0.1$ ,  $X_{\text{CO}}$  eventually reaches  $X_{\text{CO,MW}}$  at the highest  $N_{\text{H}_2}$ . In fact, if we plot  $X_{\text{CO}}$  as a function of  $Z'N_{\text{H}_2}$ , as in the right panel of Fig. 9, we see that for all  $Z'$ ,  $X_{\text{CO}}$  drops to  $X_{\text{CO,MW}}$  (the horizontal grey line) at  $Z'N_{\text{H}_2} \sim 3 \times 10^{21} \text{ cm}^{-3}$ , which corresponds to a visual extinction  $A_V \sim 3$  and is where dust shielding becomes effective. This is qualitatively consistent with the cloud-scale simulations in Shetty et al. (2011a).

Fig. 10 shows the probability density functions (PDFs) of  $X_{\text{CO}}$  (left panel) and  $R_{21}$  (right panel) at different  $Z'$ . The area-weighted PDFs are shown in blue while the  $W_{10}$ -weighted PDFs are shown in orange. Most cloud area is filled by diffuse gas with high  $X_{\text{CO}}$  and low  $R_{21}$ , while most CO(1–0) emission originates from dense gas with low  $X_{\text{CO}}$  and high  $R_{21}$ .

As  $X_{\text{CO}}$  is a distribution rather than a constant, if we want choose a statistical quantity to represent the distribution, a natural choice would be the  $W_{10}$ -weighted average (as shown by the red horizontal bars):

$$\langle X_{\text{CO}} \rangle_W \equiv \frac{\int X_{\text{CO}} W_{10} da}{\int W_{10} da} = \frac{\sum_i X_{\text{CO},i} W_{10,i}}{\sum_i W_{10,i}}, \quad (30)$$

where the summation is over the  $512^2$  beams. On the other hand, the conversion factor in a coarse beam of size  $l_b$  can be expressed as

$$X_{\text{CO}}(l_b) = \frac{N_{\text{H}_2}(l_b)}{W_{10}(l_b)} = \frac{\sum_i N_{\text{H}_2,i}}{\sum_i W_{10,i}} = \frac{\sum_i X_{\text{CO},i} W_{10,i}}{\sum_i W_{10,i}}, \quad (31)$$

where the summation is over all sub-beams within a coarse beam. Therefore,  $\langle X_{\text{CO}} \rangle_W$  is also the global conversion factor for the entire  $(1 \text{ kpc})^2$  area shown in Fig. 1. Similarly, the global  $W_{10}$ -weighted average of  $R_{21}$  (red horizontal bars) is

$$\langle R_{21} \rangle_W \equiv \frac{\int R_{21} W_{10} da}{\int W_{10} da} = \frac{\sum_i R_{21,i} W_{10,i}}{\sum_i W_{10,i}}. \quad (32)$$

Since the line ratio in a coarse beam of size ( $l_b$ ) can be written as

$$R_{21}(l_b) = \frac{W_{21}(l_b)}{W_{10}(l_b)} = \frac{\sum_i W_{21,i}}{\sum_i W_{10,i}} = \frac{\sum_i R_{21,i} W_{10,i}}{\sum_i W_{10,i}}, \quad (33)$$

where the summation is over all sub-beams within a coarse beam,  $\langle R_{21} \rangle_W$  is also the global line ratio for the entire  $(1 \text{ kpc})^2$  area.

## 5.2. Scale Dependence

The left panels in Fig. 11 show the relationships between  $N_{\text{H}_2}$  and  $N_{\text{CO}}$  at different beam sizes for  $Z' = 1$ . The dashed grey lines indicate  $N_{\text{CO}} = 2N_{\text{H}_2}x_{\text{C},0}$ , which is the upper limit of  $N_{\text{CO}}$  when carbon is completely in form of CO.

On large scales, a coarse beam contains a distribution of  $N_{\text{H}_2}$  and  $N_{\text{CO}}$ , and the CO-to- $\text{H}_2$  ratio can be expressed as

$$\gamma(l_b) = \frac{N_{\text{CO}}(l_b)}{N_{\text{H}_2}(l_b)} = \frac{\sum_i N_{\text{CO},i}}{\sum_i N_{\text{H}_2,i}} = \frac{\sum_i \gamma_i N_{\text{H}_2,i}}{\sum_i N_{\text{H}_2,i}}, \quad (34)$$

where the summation is over all sub-beams within a coarse beam. Namely, the coarse-beam  $\gamma$  is the  $N_{\text{H}_2}$ -weighted average of the small-scale  $\gamma$  over the sub-beam distribution and the dense, CO-rich gas (where  $\gamma$  is high) has a dominant contribution to the coarse-beam  $\gamma$ . Since  $\gamma$  increases monotonically with  $N_{\text{H}_2}$ , the coarse-beam  $\gamma$  increases with  $l_b$  at a given  $N_{\text{H}_2}$ . In addition, the variation of  $\gamma$  decreases as  $l_b$  increases because of beam averaging/smoothing.

Qualitatively, the  $N_{\text{H}_2}$ – $W_{10}$  relation, which we show in the right panels of Fig. 11, is very similar to the  $N_{\text{H}_2}$ – $N_{\text{CO}}$  relation. The solid, dotted and dash-dotted lines in grey indicate  $X_{\text{CO}}/X_{\text{CO,MW}} = 1, 10, \text{ and } 100$ , respectively. Recall that the conversion factor in a coarse beam is the  $W_{10}$ -weighted average of the small-scale  $X_{\text{CO}}$  over the sub-beam distribution. If  $X_{\text{CO}}$  is constant within a coarse beam (even if  $N_{\text{H}_2}$  and  $W_{10}$  are not constant), the coarse-beam conversion factor is unchanged. However, if there is a sub-beam distribution of  $X_{\text{CO}}$ , Eq. (31) implies that the dense, CO-bright gas (where  $X_{\text{CO}}$  is low) has a dominant contribution to the coarse-beam  $X_{\text{CO}}$ . Since  $W_{10}$  is a super-linear function of  $N_{\text{H}_2}$  (i.e.,  $X_{\text{CO}}$  decreases as  $N_{\text{H}_2}$  increases), the coarse-beam conversion factor decreases with  $l_b$  at a given  $N_{\text{H}_2}$ . In addition, the variation of  $X_{\text{CO}}$  decreases as  $l_b$  increases because of the smoothing/averaging.

As  $l_b$  decreases, the  $N_{\text{H}_2}$ – $W_{10}$  relationship gradually converges. Convergence occurs when  $l_b$  is small enough such that  $X_{\text{CO}}$  is constant within each beam. To achieve this, the transition regions where  $X_{\text{CO}}$  varies most have

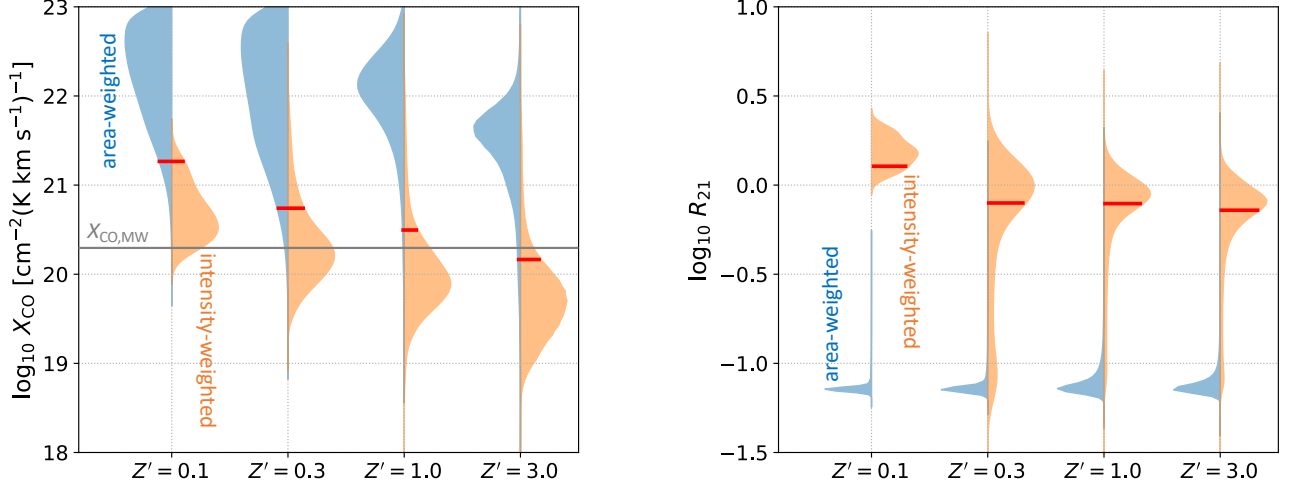


**Figure 10.** Probability density functions (PDFs) of  $X_{\text{CO}}$  (left panel) and  $R_{21}$  (right panel) at different  $Z'$ . The area-weighted PDFs are shown in blue while the  $W_{10}$ -weighted PDFs are shown in orange. The  $W_{10}$ -weighted average of  $X_{\text{CO}}$  (Eq. (30)) and  $R_{21}$  (Eq. (32)) are indicated by the red bars. The Milky-Way value of  $X_{\text{CO}}$  is shown by the horizontal grey line. Most cloud area is filled by diffuse gas with high  $X_{\text{CO}}$  and low  $R_{21}$ , while most CO(1–0) emission originates from dense gas with low  $X_{\text{CO}}$  and high  $R_{21}$ .

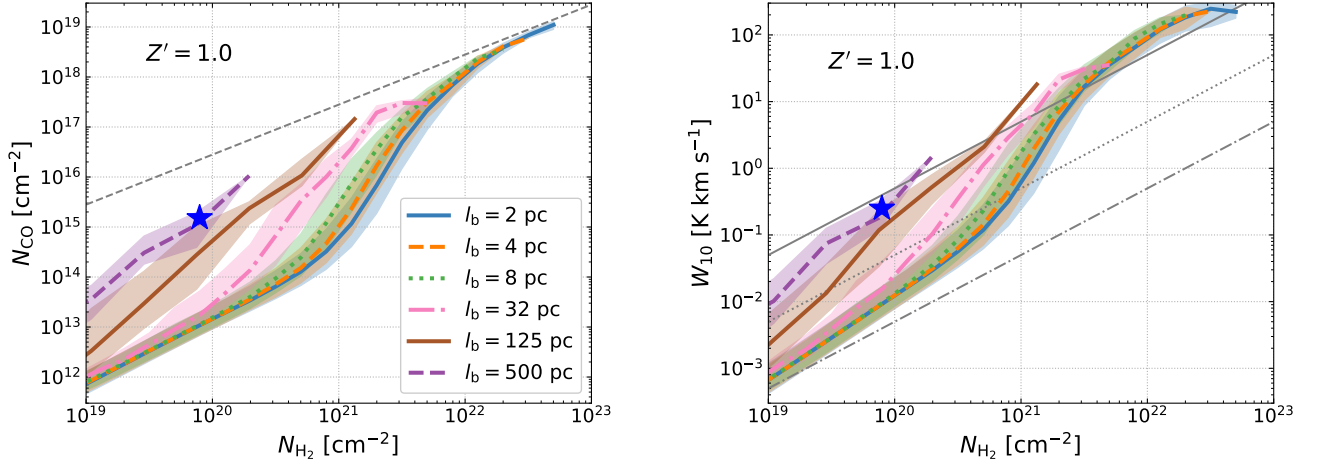


**Figure 11.** *Left:* Relationships between  $N_{\text{H}_2}$  and  $N_{\text{CO}}$  at different beam sizes ( $l_b$ ) for  $Z' = 3, 1, 0.3$ , and  $0.1$  (from top to bottom). The lines represent the median values while the shaded areas enclose the 25th and 75th percentiles. The dashed grey lines indicate  $N_{\text{CO}} = 2N_{\text{H}_2}x_{\text{C},0}$  where hydrogen and carbon are fully in the forms of  $\text{H}_2$  and  $\text{CO}$ , respectively. *Right:* Same as the left panels, but with  $W_{10}$  in the  $y$ -axis. The solid, dotted and dash-dotted lines in grey indicate  $X_{\text{CO}}/X_{\text{CO,MW}} = 1, 10$ , and  $100$ , respectively, where  $X_{\text{CO,MW}} = 2 \times 10^{20} \text{ cm}^{-2} (\text{K km s}^{-1})^{-1}$  is the canonical CO-to- $\text{H}_2$  conversion factor. The blue star symbols indicate the time-averaged values with  $l_b = 1$  kpc.

to be spatially resolved, which is increasingly challenging as  $Z'$  decreases since the CO-bright clouds becomes smaller.

To make connections with observables, we show  $X_{\text{CO}}$  as a function of  $W_{10}$  in the left panels of Fig. 12. The blue star symbol indicates the time-averaged global ( $l_b = 1$  kpc) value. On small scales,  $X_{\text{CO}}$  varies by orders of magnitude. The observed variation depends on the detection threshold. If the threshold intensity  $W_{10,\text{th}}$

is high (i.e., low sensitivity), the variation of  $X_{\text{CO}}$  is reduced as only the brightest regions with low  $X_{\text{CO}}$  can be

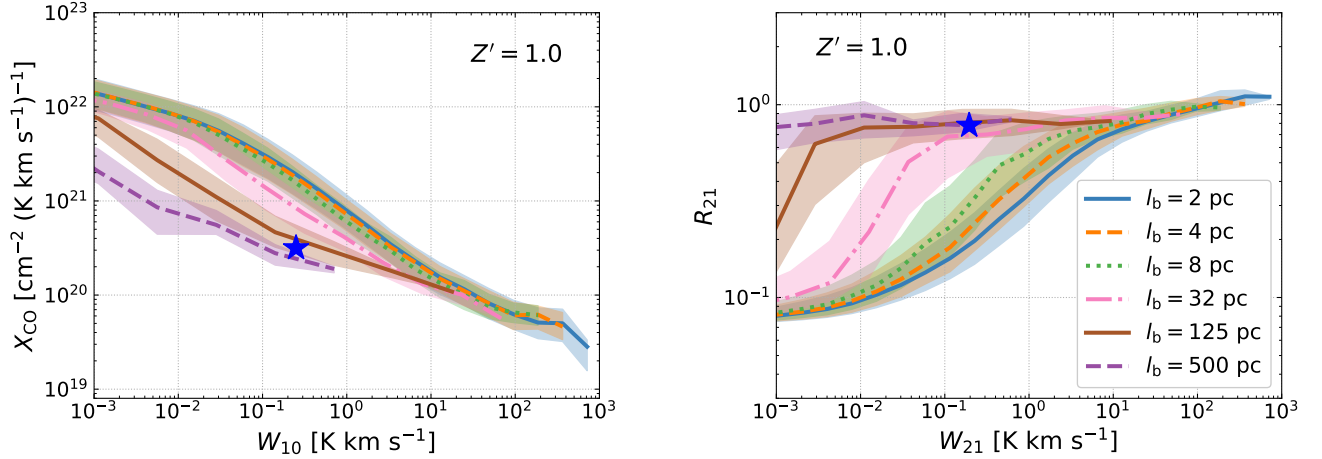


**Figure 12.** *Left:*  $X_{\text{CO}}$  as a function of  $W_{10}$  with different beam sizes ( $l_b$ ) for  $Z' = 3, 1, 0.3,$  and  $0.1$  (from top to bottom). The lines represent the median values while the shaded areas enclose the 25th and 75th percentiles. *Right:* Same as the left panels, but showing the line ratio ( $R_{21} \equiv W_{21}/W_{10}$ ) as a function of  $W_{21}$ . The blue star symbols indicate the time-averaged values with  $l_b = 1$  kpc.

detected while the diffuse gas becomes “CO-dark.”<sup>5</sup> On the other hand, if we adopt a much lower  $W_{10,\text{th}}$  (i.e., better sensitivity),  $X_{\text{CO}}$  can vary by more than an order of magnitude as both low- and high- $X_{\text{CO}}$  regions are detected. In this case, adopting a constant  $X_{\text{CO}}$  (which is typically done in observations) implies that  $N_{\text{H}_2}$  would be substantially underestimated in diffuse gas and overestimated in dense gas. In other words, the gradient of  $N_{\text{H}_2}$  would be overestimated.

As  $l_b$  decreases,  $X_{\text{CO}}$  becomes increasingly uniform due to beam averaging and eventually approaches the global value. For example, at  $l_b = 125$  pc,  $X_{\text{CO}}$  only varies by a factor of two above  $W_{10} = 1$  K km s<sup>-1</sup>.

The scale dependence of  $R_{21}$  can be understood in a similar way, as shown in the right panels of Fig. 12.  $R_{21}$  in a coarse beam is the  $W_{10}$ -weighted average of the small-scale  $R_{21}$  over the sub-beam distribution and the dense, thermalized gas (where  $R_{21}$  is high) has a dominant contribution to the coarse-beam  $R_{21}$ . Since  $R_{21}$  increases monotonically with  $W_{10}$ , the coarse-beam  $R_{21}$  increases with  $l_b$ . The variation of  $R_{21}$  decreases as  $l_b$  increases because of the smoothing/averaging and eventually  $R_{21}$  approaches the global average at  $l_b = 1$  kpc (blue star symbol).

Figs. 11 and 12 focus exclusively on solar metallicity. In Fig. 13, we show  $X_{\text{CO}}$  as a function of  $W_{10}$  for dif-

ferent  $Z'$  (colored lines) and different  $l_b$  (panels). The time-averaged global ( $l_b = 1$  kpc) values are shown in stars. On small scales ( $l_b = 2$  pc),  $X_{\text{CO}}$  is a decreasing function of  $W_{10}$  with a secondary dependence on  $Z'$  most prominent at  $W_{10} > 1$  K km s<sup>-1</sup>. As  $l_b$  increases, the  $W_{10}$ - $X_{\text{CO}}$  relation is shifted downward and rightward. Moreover, the secondary dependence on  $Z'$  is gradually reduced for a given  $W_{10}$ . At  $l_b = 1$  kpc, a single power-law relation holds for all  $Z'$ , with different  $Z'$  populating different ranges of  $W_{10}$ . We provide the best-fit formula shown as the red dashed line:

$$X_{\text{CO}} = 8.95 \times 10^{19} \left( \frac{W_{10}}{\text{K km s}^{-1}} \right)^{-0.43} \text{ cm}^{-2} (\text{K km s}^{-1})^{-1}, \quad (35)$$

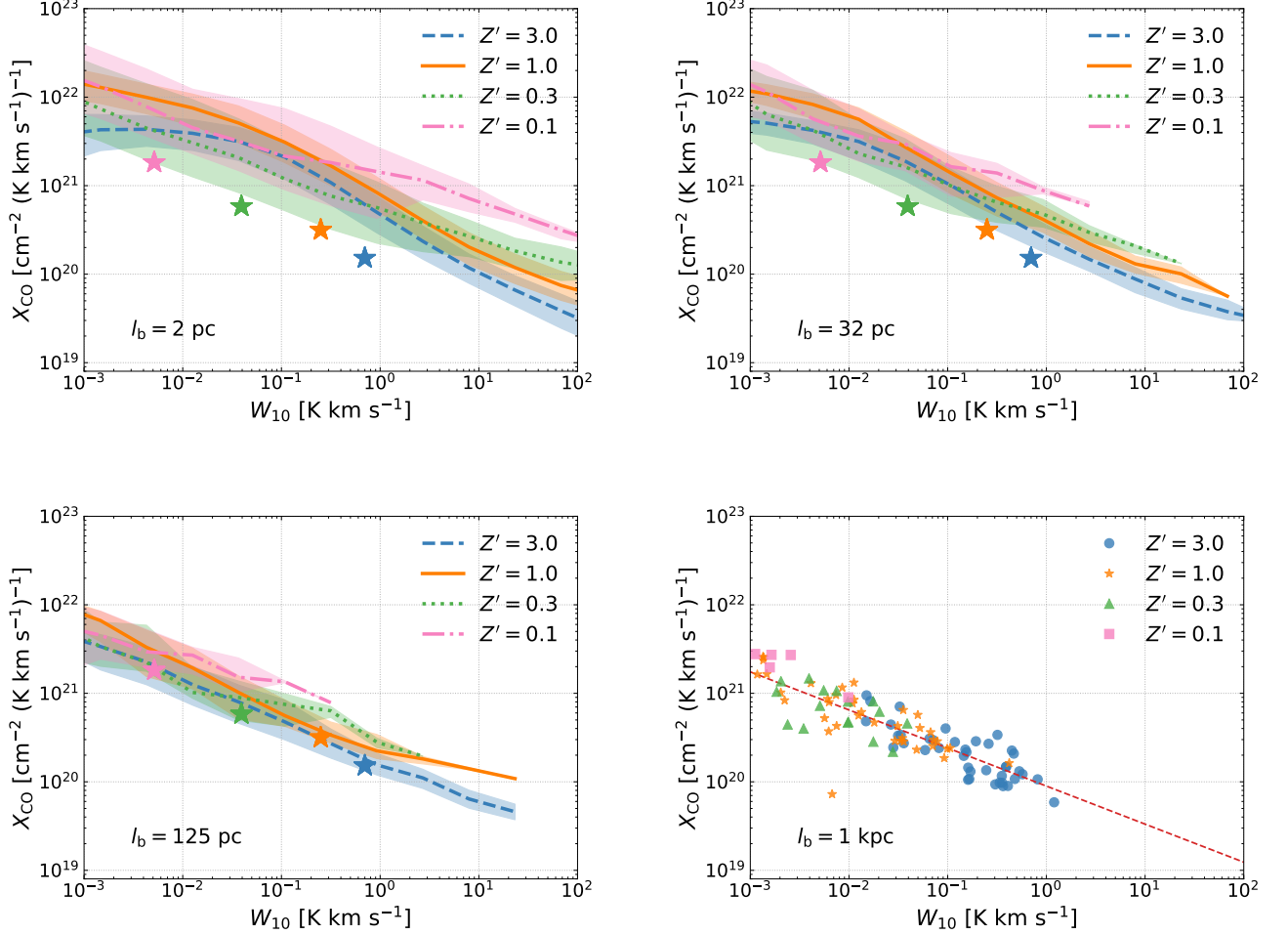
with a correlation coefficient of 0.90.

Fig. 13 summarizes the key result of this paper and can be used to more accurately infer the  $\text{H}_2$  mass from CO(1-0) observations. It highlights the fact that  $X_{\text{CO}}$  depends not only on  $Z'$ , but also on  $W_{10}$  and  $l_b$ . Different observations probe different regimes of the parameter space, leading to discrepancies when projecting on the  $Z'$ - $X_{\text{CO}}$  plane. For example, observations using the dust-based method or the inverse KS method typically have kpc-scale beam sizes within which the diffuse and dense gas are averaged over, while high-resolution CO observations (the virial method) are naturally biased towards the dense gas as the diffuse gas might be below the detection threshold.

### 5.3. CO-dark $\text{H}_2$ Fraction

The left panel of Fig. 14 shows the cumulative distributions of  $W_{10}$  weighted by  $N_{\text{H}_2}$  (solid) and  $W_{10}$  (dashed), respectively. Most CO(1-0) emission is coming from  $1 < W_{10} < 100$  K km s<sup>-1</sup>, while the  $\text{H}_2$  mass

<sup>5</sup> Note that we adopt an observational definition of “CO-dark.” Namely, we distinguish between “CO-dark” gas and “high- $X_{\text{CO}}$ ” gas. The former solely reflects the detectability controlled by the detection threshold  $W_{10,\text{th}}$  and is, in principle, independent of  $X_{\text{CO}}$ . Gas with low  $X_{\text{CO}}$  can be CO-dark if  $W_{10,\text{th}}$  is high. Conversely, Gas with high  $X_{\text{CO}}$  can also be CO-bright if  $W_{10,\text{th}}$  is low enough to detect it.



**Figure 13.**  $X_{\text{CO}}$  as a function of  $W_{10}$  for different  $Z'$  (colored lines) and different  $l_b$  (panels). The lines represent the median values while the shaded areas enclose the 25th and 75th percentiles. The time-averaged global values are shown by the star symbols. The bottom right panel is shown with a scatter plot due to limited data points at  $l_b = 1$  kpc. The  $W_{10} - X_{\text{CO}}$  relation at  $l_b = 1$  kpc can be well-described by a single power law (red dashed line, Eq. (35)) for all metallicities. This figure can be used to more accurately infer  $\text{H}_2$  mass observationally.

is distributed in a lower and more widespread range  $10^{-2} < W_{10} < 10$  K km s $^{-1}$ . This difference makes CO(1-0) an imperfect tracer of  $\text{H}_2$ . The  $N_{\text{H}_2}$ -weighted cumulative distribution can also be interpreted as the CO-dark  $\text{H}_2$  mass fraction

$$F_{\text{dark}}^m \equiv \frac{M_{\text{H}_2}(W_{10} < W_{10,\text{th}})}{M_{\text{H}_2}} \quad (36)$$

as a function of detection threshold ( $W_{10,\text{th}}$ ). Adopting  $W_{10,\text{th}} = 1$  K km s $^{-1}$ , the CO-dark  $\text{H}_2$  mass fraction is about 55% to 75% from  $Z' = 3$  to 0.1, consistent with HSvD21 where we adopted an  $N_{\text{CO}}$ -equivalent threshold. More than half of the  $\text{H}_2$  mass is hidden in the undetected diffuse gas. Similarly, the  $W_{10}$ -weighted cumulative distribution can be interpreted as the CO-dark

light fraction

$$F_{\text{dark}}^l \equiv \frac{L_{10}(W_{10} < W_{10,\text{th}})}{L_{10}} \quad (37)$$

as a function of detection threshold ( $W_{10,\text{th}}$ ). For  $W_{10,\text{th}} = 1$  K km s $^{-1}$ , the CO-dark light fraction is about 5% to 20% from  $Z' = 3$  to 0.1, i.e., most of the CO(1-0) emission can be detected.

Correspondingly, the intensity-weighted average conversion factor over the detectable beams (i.e.,  $W_{10} \geq W_{10,\text{th}}$ ) as a function of  $Z'$  is shown in the right panel of Fig. 14. The Milky Way value  $X_{\text{CO},\text{MW}}$  is shown by the horizontal red line. As the CO-bright  $\text{H}_2$  mass fraction is  $1 - F_{\text{dark}}^m$  and the CO-bright light fraction is  $1 - F_{\text{dark}}^l$ , the intensity-weight conversion factor above a detection

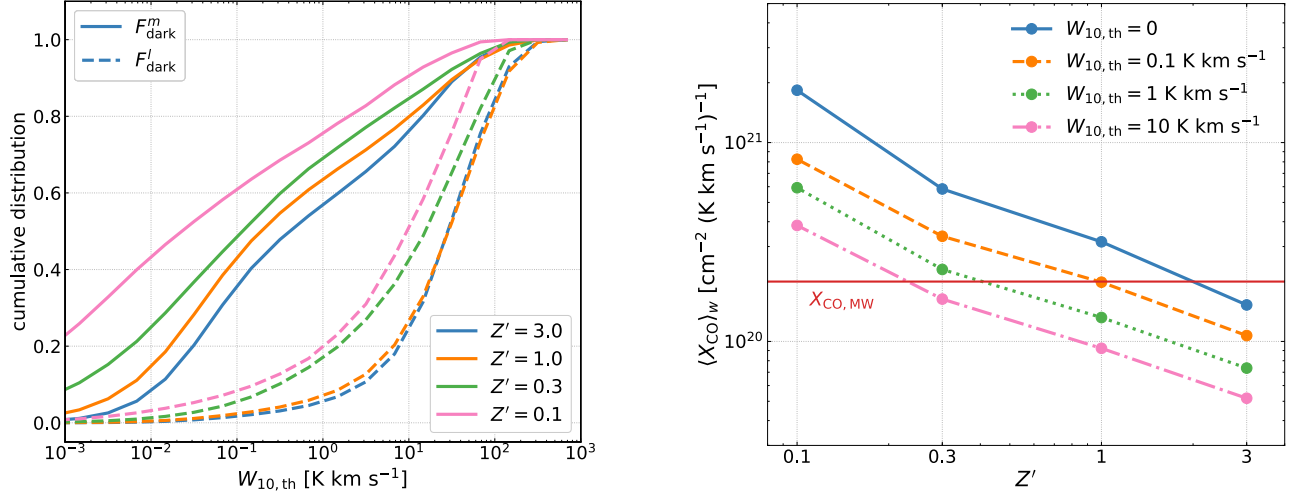


**Figure 14.** *Left:* CO-dark H<sub>2</sub> mass fraction (solid) and CO-dark light fraction (dashed) as a function of detection threshold  $W_{10,\text{th}}$ . *Right:* Intensity-weighted average  $X_{\text{CO}}$  as a function of  $Z'$  with different detection thresholds. The horizontal line shows the Milky Way value  $X_{\text{CO},\text{MW}}$ . A higher detection threshold leads to a lower  $X_{\text{CO},\text{MW}}$  as only the brightest gas with low  $X_{\text{CO}}$  can be detected.

threshold  $W_{10,\text{th}}$  follows

$$\begin{aligned} \langle X_{\text{CO}}(W_{10} \geq W_{10,\text{th}}) \rangle_W &= \frac{1 - F_{\text{dark}}^m}{1 - F_{\text{dark}}^l} \langle X_{\text{CO}} \rangle_W \\ &\approx (1 - F_{\text{dark}}^m) \langle X_{\text{CO}} \rangle_W, \quad (38) \end{aligned}$$

where the approximation holds when most of the CO(1–0) emission can be detected (i.e.,  $1 - F_{\text{dark}}^l \approx 1$ ). For example, if we adopt  $W_{10,\text{th}} = 1 \text{ K km s}^{-1}$ , then  $F_{\text{dark}}^m \approx 60\%$ ,  $F_{\text{dark}}^l \approx 5\%$ , and thus  $\langle X_{\text{CO}}(W_{10} \geq 1 \text{ K km s}^{-1}) \rangle_W \approx 0.42 \langle X_{\text{CO}} \rangle_W$ . In general, a higher detection threshold leads to a lower value as only the brightest gas with low  $X_{\text{CO}}$  can be detected.

Table 1 summarizes several global intensity-weighted average quantities.

## 6. SUMMARY

We have studied the CO-to-H<sub>2</sub> conversion factor and the line ratio of CO(2–1) to CO(1–0) in high-resolution ( $\sim 0.2 \text{ pc}$ ) hydrodynamical simulations of a multiphase ISM across a wide range of metallicity ( $0.1 \leq Z' \leq 3$ ) in HSvD21. We use the radiative transfer code RADMC-3D to post-process CO emission over a 400 Myr time period such that a large number of clouds at different evolutionary stages are properly sampled. We interpolate the particle data onto an adaptive mesh (the code is publicly available<sup>6</sup>) with a minimum cell size of  $\sim 0.2 \text{ pc}$  to ensure that all small-scale CO emission is properly captured in our radiative transfer calculations, which is

<sup>6</sup> <https://github.com/huchiayu/ParticleGridMapper.jl>

**Table 1.** Global intensity-weighted average quantities.

$Z'$	$\langle X_{\text{CO}} \rangle_W$	$\langle R_{21} \rangle_W$	$\langle \tau_{10} \rangle_W$	$\langle \tau_{21} \rangle_W$	$\langle \overline{T}_{\text{exc},s} \rangle_W$
(1)	(2)	(3)	(4)	(5)	(6)
3	$1.52 \times 10^{20}$	0.71	39.0	99.3	11.4
1	$3.17 \times 10^{20}$	0.78	15.5	42.8	12.3
0.3	$5.84 \times 10^{20}$	0.79	3.38	10.8	10.6
0.1	$1.83 \times 10^{21}$	1.29	0.31	1.38	–

NOTE— (1) Normalized metallicity. (2) CO-to-H<sub>2</sub> conversion factor in units of  $\text{cm}^{-2} (\text{K km s}^{-1})^{-1}$ . (3) Line ratio of CO(2–1) to CO(1–0). (4) Optical depth of CO(1–0). (5) Optical depth of CO(2–1) (weighted by  $W_{21}$  instead of  $W_{10}$ ). (6) Cloud surface excitation temperature of CO(1–0) in units of K assuming optically thick conditions (see Eq. 25). It is absent in the  $Z' = 0.1$  case as CO(1–0) is always optically thin even in the densest gas.

particularly important at low metallicities. Our main findings can be summarized as follows:

1. The kpc-scale  $X_{\text{CO}}$  at low  $Z'$  can be overestimated either by assuming steady-state chemistry (e.g., when converting fine structure metal lines and CO lines to an H<sub>2</sub> mass via PDR models) or by assuming the star-forming gas is fully molecular (e.g., when using the inverse KS method to convert an SFR to an H<sub>2</sub> mass) (see Fig. 1). Our fiducial, time-dependent model can be described by Eq. (8) on 1 kpc scale.



2. Instead of a single-variable function of  $Z'$ ,  $X_{\text{CO}}$  is a multivariate function of three observables:  $Z'$ ,  $W_{10}$ , and  $l_b$  (Fig. 13). Observations with different beam sizes and detection thresholds are sensitive to different parts of the parameter space. Comparing  $X_{\text{CO}}$  between different observations on the  $Z' - X_{\text{CO}}$  plane can therefore be misleading, and a fair comparison should take all three variables into account.
3. On large scales, the metallicity dependence on the  $W_{10} - X_{\text{CO}}$  plane is gradually reduced as a result of the sub-beam gas distribution. At  $l_b = 1$  kpc, a single power-law relation (Eq. (35)) holds for all  $Z'$ , with different  $Z'$  populating different ranges of  $W_{10}$  (Fig. 13).
4. On parsec scales,  $X_{\text{CO}}$  varies by orders of magnitude from place to place. The variation of  $X_{\text{CO}}$  occurs primarily in the optically thin regime, driven by the variation of CO abundance in the transition from atomic carbon to CO. The pc-scale  $X_{\text{CO}}$  can be well-characterized by a single parameter  $Z'N_{\text{H}_2}$ , and it drops to the Milky Way value once dust shielding becomes effective (Fig. 9).
5. The line intensities are proxies of column or volume densities and thus can be used to infer  $X_{\text{CO}}$  and  $R_{21}$ . On pc-scales,  $X_{\text{CO}}$  negatively correlates with  $W_{10}$  while  $R_{21}$  positively correlates with  $W_{21}$  (Fig. 12). The large-scale  $X_{\text{CO}}$  and  $R_{21}$  are results of beam averaging, and they are naturally biased towards values in dense gas with low  $X_{\text{CO}}$  and high  $R_{21}$  (Eqs. (31) and (33)).
6. Most cloud area is filled by diffuse gas with high  $X_{\text{CO}}$  and low  $R_{21}$ , while most CO emission originates from dense gas with low  $X_{\text{CO}}$  and high  $R_{21}$  (Fig. 10). Adopting a constant  $X_{\text{CO}}$  strongly over-(under-)estimates  $\text{H}_2$  in dense (diffuse) gas.
7. Both CO(1–0) and CO(2–1) are thermalized at higher densities as  $Z'$  decreases (Fig. 6) because (i)  $\text{H}_2$  exists at densities higher than the critical densities of the lines, and (ii) the CO abundances and hence the optical depth are lower which leads to less radiation trapping.
8. The l.o.s. average gas density increases with  $N_{\text{CO}}$ . In addition, as CO only exists at the densest core at low  $Z'$ , the corresponding l.o.s. average gas density is higher at a given  $N_{\text{CO}}$ . This effect counters

the higher thermalization densities such that the CO levels are more efficiently excited at low  $Z'$  (Fig. 7).

9. The CO lines become increasingly optically thin at lower  $Z'$ . This is not only because of the lower CO column densities but also because the levels are more efficiently excited, which leads to a smaller optical depth at a given  $N_{\text{CO}}$  (Fig. 7). In the optically thick regime, the line intensities increase faster than  $\ln N_{\text{CO}}$  (as the curve of growth theory would predict) because the excitation temperature also increases with  $N_{\text{CO}}$  and gradually approaches the kinetic temperature due to the increase in the l.o.s. average density.
10. The excitation temperature derived from the peak radiation temperature (Eq. (25)) is sub-thermal (Fig. 8 and Table 1). At  $Z' = 0.1$ , Eq. (25) is no longer applicable as the optically thick assumption breaks down. In addition,  $R_{21}$  increases as the lines become increasingly optically thin.
11. The intensity-weighted average  $X_{\text{CO}}$  is controlled by the CO-dark  $\text{H}_2$  mass fraction and the CO-dark light fraction (Fig. 14 and Eq. (38)), and it decreases with the detection threshold  $W_{10,\text{th}}$  as only the brightest gas with low  $X_{\text{CO}}$  can be detected.

To sum up,  $X_{\text{CO}}$  is a multivariate function of metallicity, line intensity, and beam size. Although we did not find a simple parametrization for this function, our Fig. 13 can be used by observers to more accurately infer the  $\text{H}_2$  mass in galaxies with similar conditions of the solar neighborhood. It is still unclear to what extent this function is applicable in different environments (e.g., high-redshift galaxies, dwarf galaxies, etc.) where the large-scale physical properties (e.g., gas surface density, turbulence, etc.) are very different. This will be investigated in followup studies.

#### ACKNOWLEDGMENTS

We thank the anonymous referee for the constructive comments that improved our manuscript. C.Y.H. acknowledges support from the DFG via German-Israel Project Cooperation grant STE1869/2-1 GE625/17-1. A.S. thanks the Center for Computational Astrophysics (CCA) of the Flatiron Institute, and the Mathematics and Physical Science (MPS) division of the Simons Foundation for support. All simulations were run on the Raven, Cobra and Draco supercomputers at the Max Planck Computing and Data Facility (MPCDF).

## REFERENCES

- Accurso, G., Saintonge, A., Catinella, B., et al. 2017, *MNRAS*, 470, 4750, doi: [10.1093/mnras/stx1556](https://doi.org/10.1093/mnras/stx1556)
- Amorín, R., Muñoz-Tuñón, C., Aguerra, J. A. L., & Planesas, P. 2016, *A&A*, 588, A23, doi: [10.1051/0004-6361/201526397](https://doi.org/10.1051/0004-6361/201526397)
- Barnes, J., & Hut, P. 1986, *Nature*, 324, 446, doi: [10.1038/324446a0](https://doi.org/10.1038/324446a0)
- Bialy, S., & Sternberg, A. 2019, *ApJ*, 881, 160, doi: [10.3847/1538-4357/ab2fd1](https://doi.org/10.3847/1538-4357/ab2fd1)
- Bisbas, T. G., Tan, J. C., & Tanaka, K. E. I. 2021, *MNRAS*, 502, 2701, doi: [10.1093/mnras/stab121](https://doi.org/10.1093/mnras/stab121)
- Bisbas, T. G., van Dishoeck, E. F., Papadopoulos, P. P., et al. 2017, *ApJ*, 839, 90, doi: [10.3847/1538-4357/aa696d](https://doi.org/10.3847/1538-4357/aa696d)
- Bolatto, A. D., Jackson, J. M., & Ingalls, J. G. 1999, *ApJ*, 513, 275, doi: [10.1086/306849](https://doi.org/10.1086/306849)
- Bolatto, A. D., Leroy, A. K., Rosolowsky, E., Walter, F., & Blitz, L. 2008, *ApJ*, 686, 948, doi: [10.1086/591513](https://doi.org/10.1086/591513)
- Bolatto, A. D., Wolfire, M., & Leroy, A. K. 2013, *ARA&A*, 51, 207, doi: [10.1146/annurev-astro-082812-140944](https://doi.org/10.1146/annurev-astro-082812-140944)
- Clark, P. C., Glover, S. C. O., & Klessen, R. S. 2012, *MNRAS*, 420, 745, doi: [10.1111/j.1365-2966.2011.20087.x](https://doi.org/10.1111/j.1365-2966.2011.20087.x)
- Cormier, D., Madden, S. C., Lebouteiller, V., et al. 2014, *A&A*, 564, A121, doi: [10.1051/0004-6361/201322096](https://doi.org/10.1051/0004-6361/201322096)
- den Brok, J. S., Chatzigiannakis, D., Bigiel, F., et al. 2021, *MNRAS*, 504, 3221, doi: [10.1093/mnras/stab859](https://doi.org/10.1093/mnras/stab859)
- Draine, B. T. 1978, *ApJS*, 36, 595, doi: [10.1086/190513](https://doi.org/10.1086/190513)
- . 2011, *Physics of the Interstellar and Intergalactic Medium*
- Duarte-Cabral, A., Acreman, D. M., Dobbs, C. L., et al. 2015, *MNRAS*, 447, 2144, doi: [10.1093/mnras/stu2586](https://doi.org/10.1093/mnras/stu2586)
- Dullemond, C. P., Juhasz, A., Pohl, A., et al. 2012, *RADMC-3D: A multi-purpose radiative transfer tool*. <http://ascl.net/1202.015>
- Ekström, S., Georgy, C., Eggenberger, P., et al. 2012, *A&A*, 537, A146, doi: [10.1051/0004-6361/201117751](https://doi.org/10.1051/0004-6361/201117751)
- Elmegreen, B. G., Rubio, M., Hunter, D. A., et al. 2013, *Nature*, 495, 487, doi: [10.1038/nature11933](https://doi.org/10.1038/nature11933)
- Feldmann, R., Gnedin, N. Y., & Kravtsov, A. V. 2012, *ApJ*, 747, 124, doi: [10.1088/0004-637X/747/2/124](https://doi.org/10.1088/0004-637X/747/2/124)
- Flower, D. R. 2001, *Journal of Physics B Atomic Molecular Physics*, 34, 2731, doi: [10.1088/0953-4075/34/13/315](https://doi.org/10.1088/0953-4075/34/13/315)
- Fuchs, B., Jahreiß, H., & Flynn, C. 2009, *AJ*, 137, 266, doi: [10.1088/0004-6256/137/1/266](https://doi.org/10.1088/0004-6256/137/1/266)
- Gaburov, E., & Nitadori, K. 2011, *MNRAS*, 414, 129, doi: [10.1111/j.1365-2966.2011.18313.x](https://doi.org/10.1111/j.1365-2966.2011.18313.x)
- Gatto, A., Walch, S., Naab, T., et al. 2017, *MNRAS*, 466, 1903, doi: [10.1093/mnras/stw3209](https://doi.org/10.1093/mnras/stw3209)
- Genzel, R., Tacconi, L. J., Combes, F., et al. 2012, *ApJ*, 746, 69, doi: [10.1088/0004-637X/746/1/69](https://doi.org/10.1088/0004-637X/746/1/69)
- Glover, S. C. O., & Clark, P. C. 2012a, *MNRAS*, 426, 377, doi: [10.1111/j.1365-2966.2012.21737.x](https://doi.org/10.1111/j.1365-2966.2012.21737.x)
- . 2012b, *MNRAS*, 421, 116, doi: [10.1111/j.1365-2966.2011.20260.x](https://doi.org/10.1111/j.1365-2966.2011.20260.x)
- Glover, S. C. O., & Mac Low, M.-M. 2007, *ApJS*, 169, 239, doi: [10.1086/512238](https://doi.org/10.1086/512238)
- . 2011, *MNRAS*, 412, 337, doi: [10.1111/j.1365-2966.2010.17907.x](https://doi.org/10.1111/j.1365-2966.2010.17907.x)
- Gong, M., Ostriker, E. C., & Kim, C.-G. 2018, *ApJ*, 858, 16, doi: [10.3847/1538-4357/aab9af](https://doi.org/10.3847/1538-4357/aab9af)
- Gong, M., Ostriker, E. C., Kim, C.-G., & Kim, J.-G. 2020, *ApJ*, 903, 142, doi: [10.3847/1538-4357/abbdab](https://doi.org/10.3847/1538-4357/abbdab)
- Górski, K. M., & Hivon, E. 2011, *HEALPix: Hierarchical Equal Area isoLatitude Pixelization of a sphere*, *Astrophysics Source Code Library*. <http://ascl.net/1107.018>
- Heays, A. N., Bosman, A. D., & van Dishoeck, E. F. 2017, *A&A*, 602, A105, doi: [10.1051/0004-6361/201628742](https://doi.org/10.1051/0004-6361/201628742)
- Hopkins, P. F. 2015, *MNRAS*, 450, 53, doi: [10.1093/mnras/stv195](https://doi.org/10.1093/mnras/stv195)
- Hu, C.-Y., Naab, T., Glover, S. C. O., Walch, S., & Clark, P. C. 2017, *MNRAS*, 471, 2151, doi: [10.1093/mnras/stx1773](https://doi.org/10.1093/mnras/stx1773)
- Hu, C.-Y., Sternberg, A., & van Dishoeck, E. F. 2021, *ApJ*, 920, 44, doi: [10.3847/1538-4357/ac0dbd](https://doi.org/10.3847/1538-4357/ac0dbd)
- Hunt, L. K., García-Burillo, S., Casasola, V., et al. 2015, *A&A*, 583, A114, doi: [10.1051/0004-6361/201526553](https://doi.org/10.1051/0004-6361/201526553)
- Indriolo, N., & McCall, B. J. 2012, *ApJ*, 745, 91, doi: [10.1088/0004-637X/745/1/91](https://doi.org/10.1088/0004-637X/745/1/91)
- Indriolo, N., Neufeld, D. A., Gerin, M., et al. 2015, *ApJ*, 800, 40, doi: [10.1088/0004-637X/800/1/40](https://doi.org/10.1088/0004-637X/800/1/40)
- Kroupa, P. 2001, *MNRAS*, 322, 231, doi: [10.1046/j.1365-8711.2001.04022.x](https://doi.org/10.1046/j.1365-8711.2001.04022.x)
- Lada, C. J., & Lada, E. A. 2003, *ARA&A*, 41, 57, doi: [10.1146/annurev.astro.41.011802.094844](https://doi.org/10.1146/annurev.astro.41.011802.094844)
- Lee, C., Leroy, A. K., Schnee, S., et al. 2015, *MNRAS*, 450, 2708, doi: [10.1093/mnras/stv863](https://doi.org/10.1093/mnras/stv863)
- Lejeune, T., Cuisinier, F., & Buser, R. 1997, *A&AS*, 125, doi: [10.1051/aas:1997373](https://doi.org/10.1051/aas:1997373)
- . 1998, *A&AS*, 130, 65, doi: [10.1051/aas:1998405](https://doi.org/10.1051/aas:1998405)
- Leroy, A. K., Bolatto, A., Gordon, K., et al. 2011, *ApJ*, 737, 12, doi: [10.1088/0004-637X/737/1/12](https://doi.org/10.1088/0004-637X/737/1/12)
- Leroy, A. K., Schinnerer, E., Hughes, A., et al. 2021, *ApJS*, 257, 43, doi: [10.3847/1538-4365/ac17f3](https://doi.org/10.3847/1538-4365/ac17f3)
- Madden, S. C., Poglitsch, A., Geis, N., Stacey, G. J., & Townes, C. H. 1997, *ApJ*, 483, 200, doi: [10.1086/304247](https://doi.org/10.1086/304247)
- Madden, S. C., Cormier, D., Hony, S., et al. 2020, *A&A*, 643, A141, doi: [10.1051/0004-6361/202038860](https://doi.org/10.1051/0004-6361/202038860)

- McKee, C. F., & Ostriker, E. C. 2007, *ARA&A*, 45, 565, doi: [10.1146/annurev.astro.45.051806.110602](https://doi.org/10.1146/annurev.astro.45.051806.110602)
- Narayanan, D., Krumholz, M. R., Ostriker, E. C., & Hernquist, L. 2012, *MNRAS*, 421, 3127, doi: [10.1111/j.1365-2966.2012.20536.x](https://doi.org/10.1111/j.1365-2966.2012.20536.x)
- Pak, S., Jaffe, D. T., van Dishoeck, E. F., Johansson, L. E. B., & Booth, R. S. 1998, *ApJ*, 498, 735, doi: [10.1086/305584](https://doi.org/10.1086/305584)
- Peñaloza, C. H., Clark, P. C., Glover, S. C. O., & Klessen, R. S. 2018, *MNRAS*, 475, 1508, doi: [10.1093/mnras/stx3263](https://doi.org/10.1093/mnras/stx3263)
- Peñaloza, C. H., Clark, P. C., Glover, S. C. O., Shetty, R., & Klessen, R. S. 2017, *MNRAS*, 465, 2277, doi: [10.1093/mnras/stw2892](https://doi.org/10.1093/mnras/stw2892)
- Pineda, J. E., Caselli, P., & Goodman, A. A. 2008, *ApJ*, 679, 481, doi: [10.1086/586883](https://doi.org/10.1086/586883)
- Richings, A. J., & Schaye, J. 2016, *MNRAS*, 458, 270, doi: [10.1093/mnras/stw327](https://doi.org/10.1093/mnras/stw327)
- Rubio, M., Elmegreen, B. G., Hunter, D. A., et al. 2015, *Nature*, 525, 218, doi: [10.1038/nature14901](https://doi.org/10.1038/nature14901)
- Schöier, F. L., van der Tak, F. F. S., van Dishoeck, E. F., & Black, J. H. 2005, *A&A*, 432, 369, doi: [10.1051/0004-6361:20041729](https://doi.org/10.1051/0004-6361:20041729)
- Schruba, A., Leroy, A. K., Walter, F., et al. 2012, *AJ*, 143, 138, doi: [10.1088/0004-6256/143/6/138](https://doi.org/10.1088/0004-6256/143/6/138)
- Schruba, A., Leroy, A. K., Kruijssen, J. M. D., et al. 2017, *ApJ*, 835, 278, doi: [10.3847/1538-4357/835/2/278](https://doi.org/10.3847/1538-4357/835/2/278)
- Seifried, D., Haid, S., Walch, S., Borchert, E. M. A., & Bisbas, T. G. 2020, *MNRAS*, 492, 1465, doi: [10.1093/mnras/stz3563](https://doi.org/10.1093/mnras/stz3563)
- Seifried, D., Walch, S., Girichidis, P., et al. 2017, *MNRAS*, 472, 4797, doi: [10.1093/mnras/stx2343](https://doi.org/10.1093/mnras/stx2343)
- Shetty, R., Glover, S. C., Dullemond, C. P., & Klessen, R. S. 2011a, *MNRAS*, 412, 1686, doi: [10.1111/j.1365-2966.2010.18005.x](https://doi.org/10.1111/j.1365-2966.2010.18005.x)
- Shetty, R., Glover, S. C., Dullemond, C. P., et al. 2011b, *MNRAS*, 415, 3253, doi: [10.1111/j.1365-2966.2011.18937.x](https://doi.org/10.1111/j.1365-2966.2011.18937.x)
- Shi, Y., Wang, J., Zhang, Z.-Y., et al. 2015, *ApJL*, 804, L11, doi: [10.1088/2041-8205/804/1/L11](https://doi.org/10.1088/2041-8205/804/1/L11)
- Smith, R. J., Treß, R. G., Sormani, M. C., et al. 2020, *MNRAS*, 492, 1594, doi: [10.1093/mnras/stz3328](https://doi.org/10.1093/mnras/stz3328)
- Springel, V. 2005, *MNRAS*, 364, 1105, doi: [10.1111/j.1365-2966.2005.09655.x](https://doi.org/10.1111/j.1365-2966.2005.09655.x)
- Sternberg, A., & Dalgarno, A. 1995, *ApJS*, 99, 565, doi: [10.1086/192198](https://doi.org/10.1086/192198)
- Tacconi, L. J., Genzel, R., & Sternberg, A. 2020, *ARA&A*, 58, 157, doi: [10.1146/annurev-astro-082812-141034](https://doi.org/10.1146/annurev-astro-082812-141034)
- van Dishoeck, E. F., & Black, J. H. 1988, *ApJ*, 334, 771, doi: [10.1086/166877](https://doi.org/10.1086/166877)
- Wernli, M., Valiron, P., Faure, A., et al. 2006, *A&A*, 446, 367, doi: [10.1051/0004-6361:20053919](https://doi.org/10.1051/0004-6361:20053919)
- Wolfire, M. G., Hollenbach, D., & McKee, C. F. 2010, *ApJ*, 716, 1191, doi: [10.1088/0004-637X/716/2/1191](https://doi.org/10.1088/0004-637X/716/2/1191)

## APPENDIX

A. SCALE DEPENDENCE OF  $\langle X_{\text{CO}} \rangle_W$ 

In the case of  $W_{10,\text{th}} = 0$  (i.e., infinite sensitivity), the global intensity-weighted average  $\langle X_{\text{CO}} \rangle_W$  is by construction independent of  $l_b$  as beam averaging is equivalent to the  $W_{10}$ -weighted average over the sub-beam distribution (see Eqs. (30) and (31)). However, if we consider a nonzero  $W_{10,\text{th}}$ ,  $\langle X_{\text{CO}} \rangle_W$  is only averaged over the CO-bright beams where  $W_{10} > W_{10,\text{th}}$  and thus does depend on  $l_b$ , as shown in Fig. 15. At a given  $l_b$ ,  $\langle X_{\text{CO}} \rangle_W$  decreases inversely with  $W_{10,\text{th}}$  as the faint, high  $X_{\text{CO}}$  gas becomes CO-dark and only the bright, low  $X_{\text{CO}}$  gas can be detected. With  $W_{10,\text{th}} = 0$ ,  $\langle X_{\text{CO}} \rangle_W$  is indeed (by construction) independent of  $l_b$ . With a finite  $W_{10,\text{th}}$ , there is a very mild  $l_b$ -dependence that arises from two competing effects. On one hand, a coarse beam averages over CO-bright and CO-dark gas. As CO emission predominately originates from the CO-bright gas, the coarse-beam intensity is likely to exceed the detection threshold. Namely, the entire coarse beam becomes CO-bright, which effectively includes the fine-grained CO-dark gas within the beam to the global average, leading to an increase in  $\langle X_{\text{CO}} \rangle_W$  as CO-dark gas tends to be of high  $X_{\text{CO}}$ . On the other hand, when the beam size is so large that the majority of the area is filled with CO-dark gas, the dilution effect can be strong enough such that the entire coarse beam becomes CO-dark, which effectively excludes the fine-grained CO-bright gas within the beam from the global average. Therefore, as  $l_b$  increases,  $\langle X_{\text{CO}} \rangle_W$  first increase at small  $l_b$  and then decreases at large  $l_b$ . The effect is very mild, within 30% from  $l_b = 2$  pc to  $l_b = 1$  kpc. In short,  $\langle X_{\text{CO}} \rangle_W$  mainly depends on the detection threshold (as shown in Fig. 14) and is nearly scale-independent.

Similarly, Fig. 16 demonstrates the scale-dependence of the global average line ratio  $\langle R_{21} \rangle_W$  (see Eq. (32)) with different detection thresholds  $W_{21,\text{th}}$ .  $\langle R_{21} \rangle_W$  is nearly scale-independent and it increases with  $W_{21,\text{th}}$  as  $R_{21}$  tends to be high in CO-bright gas. However, the variation is very weak, less than 20% in all cases.

## B. SCALE DEPENDENCE OF THE CO-DARK GAS

For a given  $W_{10,\text{th}}$ ,  $\langle X_{\text{CO}} \rangle_W$  only accounts for  $\text{H}_2$  in the CO-bright beams, while a significant amount of  $\text{H}_2$  may be hidden in the CO-dark beams. Fig. 17 shows the CO-dark  $\text{H}_2$  mass fraction ( $F_{\text{dark}}^m$ , upper row) and CO-dark light fraction ( $F_{\text{dark}}^l$ , lower row) as a function of detection threshold  $W_{10,\text{th}}$  at different beam sizes  $l_b$  for  $Z' = 3, 1, 0.3$ , and 0.1 from left to right. As  $l_b$  increases, the CDF becomes narrower due to beam smoothing and

gradually approaches a step function. Therefore,  $F_{\text{dark}}^m$  may increase or decrease as  $l_b$  increases, depending on the detection threshold. For  $W_{10,\text{th}} = 1 \text{ K km s}^{-1}$ ,  $F_{\text{dark}}^m$  remains almost constant at small  $l_b$  where the distribution is converged. At  $l_b \gtrsim 32$  pc,  $F_{\text{dark}}^m$  increases with  $l_b$  as the beam averaging makes the fine-grained CO-bright gas undetectable. Similarly,  $F_{\text{dark}}^l$  remains constant at small  $l_b$  and increase with  $l_b$  at  $l_b \gtrsim 32$  pc. This provides another explanation of why  $\langle X_{\text{CO}} \rangle_W$  is insensitive to  $l_b$ , as both  $F_{\text{dark}}^m$  and  $F_{\text{dark}}^l$  begin to increase at  $l_b \gtrsim 32$  pc and they cancel out (see Eq. (38)).

## C. CO(1–0) SPECTRUM

Fig. 18 shows 2500 CO(1–0) spectra randomly drawn from the  $512 \times 512$  pixels in the  $Z' = 1$  run at  $t = 420$  Myr. Gas motion leads to a variety of spectrum profiles, including Gaussian-like, skewed, saturated, or even double-peaked. Our adopted spectrum resolution ( $0.4 \text{ km s}^{-1}$ ) is sufficient to resolve the typical line width of the spectra, and our spectrum coverage ( $40 \text{ km s}^{-1}$ ) is large enough to include all the CO(1–0) emission.

## D. INTERPOLATION SCHEME

In this appendix, we compare three different interpolation schemes that map Lagrangian (particle) data onto a mesh. For a given particle distribution, where a particle  $i$  carries information of mass ( $m_i$ ), gas density ( $\rho_i$ ), smoothing length ( $h_i$ ), and a scalar field ( $A_i$ ) at location  $x_i$ . The standard SPH scheme interpolate the scalar field at location  $x_c$  as

$$\bar{A}_{\text{SPH}}(x_c) = \sum_j \frac{m_j}{\rho_j} A_j K(|x_j - x_c|, h_j), \quad (\text{D1})$$

where the summation is over the “scatter” neighboring particles  $j$ . This scheme has the drawback that a constant scalar field would be interpolated as non-constant, as  $\sum_j \frac{m_j}{\rho_j} K(|x_j - x_c|, h_j)$ , in general, does not sum up to unity. This can be remedied by the normalized SPH scheme:

$$\bar{A}_{\text{nSPH}}(x_c) = \frac{\sum_j \frac{m_j}{\rho_j} A_j K(|x_j - x_c|, h_j)}{\sum_j \frac{m_j}{\rho_j} K(|x_j - x_c|, h_j)}, \quad (\text{D2})$$

which factors out the non-unity term. Alternatively, one can use the MFM scheme:

$$\bar{A}_{\text{MFM}}(x_c) = \frac{\sum_j A_j K(|x_j - x_c|, h_j)}{\sum_j K(|x_j - x_c|, h_j)}. \quad (\text{D3})$$

Similar to the normalized SPH scheme, the MFM scheme interpolates a constant field as constant.

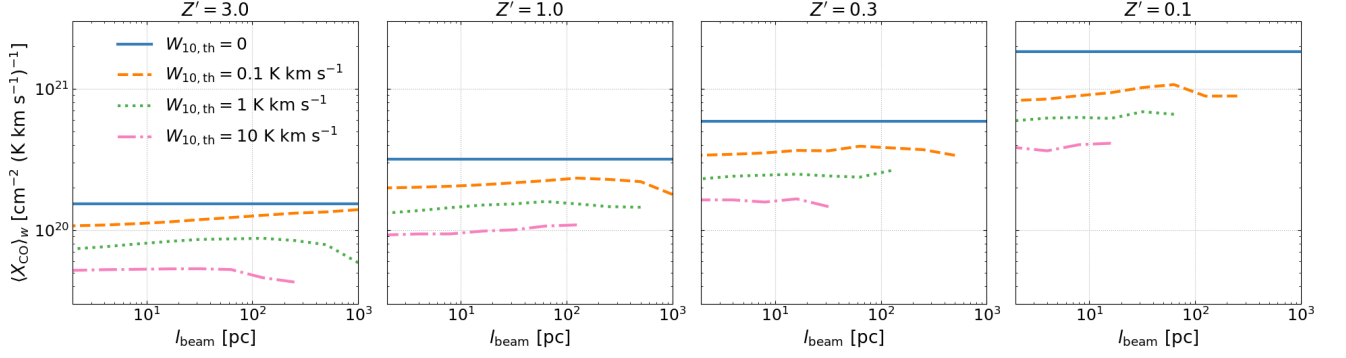


**Figure 15.** Global intensity weighted average CO-to- $\text{H}_2$  conversion factor as a function of beam size with different detection thresholds  $W_{10,\text{th}}$  at  $Z' = 3, 1, 0.3,$  and  $0.1$  from left to right.

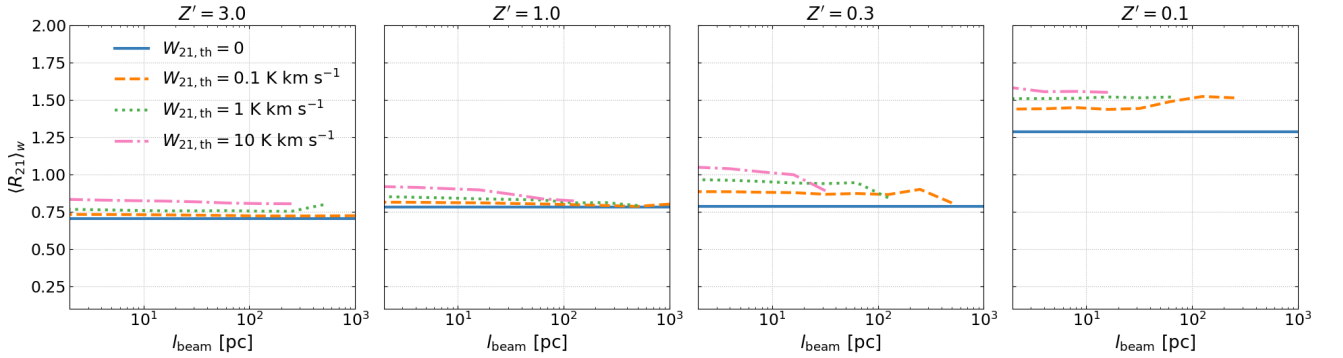


**Figure 16.** Global intensity-weighted average line ratio as a function of beam size with different detection thresholds  $W_{21,\text{th}}$  at  $Z' = 3, 1, 0.3,$  and  $0.1$  from left to right.

In Fig. 19, the left panels of show the mass-weighted PDFs of hydrogen number density ( $n$ , upper panel) and temperature ( $T$ , lower panel) for the particle data and the three interpolation schemes. The middle and right panels show the mass-weighted “phase diagram” (heatmap of  $n$  vs.  $T$ ) for the particle data and the three interpolation schemes.

While all schemes reproduce the actual density distribution from the particle data, both the standard SPH scheme and normalized SPH scheme significantly overproduce the hot gas ( $10^4 < T < 10^6$  K) and underproduce the cold gas ( $10 < T < 10^3$  K). This is caused by the volume factor  $m_j/\rho_j$  which put a strong weighting on the diffuse gas (low  $\rho_j$ ). For density interpolation, the  $\rho_j$  dependence cancels out. For temperature interpolation, as the diffuse gas typically has a high  $T$ , the contribution from the hot gas is enormous, and thus the result is generally biased high.

In contrast, the MFM scheme depends merely on particle configuration (which defines  $h_j$ ) and is independent of  $m_j$  and  $\rho_j$ . This means that the diffuse gas does not have the same strong weighting as in the SPH schemes,

and thus the temperature distribution is more faithfully reproduced.



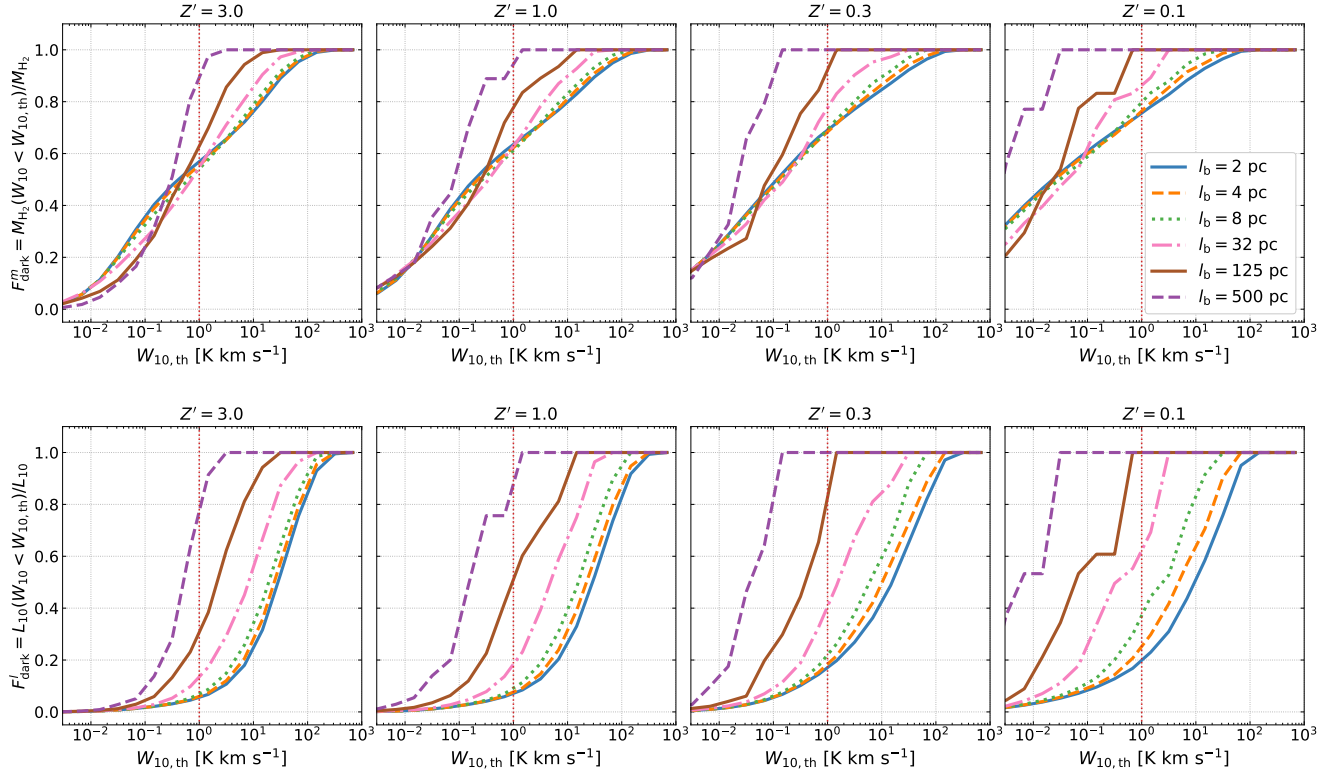


**Figure 17.** CO-dark  $H_2$  mass fraction (upper) and CO-dark light fraction (lower) as a function of detection threshold  $W_{10, \text{th}}$  at different beam sizes  $l_b$  for  $Z' = 3, 1, 0.3$ , and  $0.1$  from left to right.

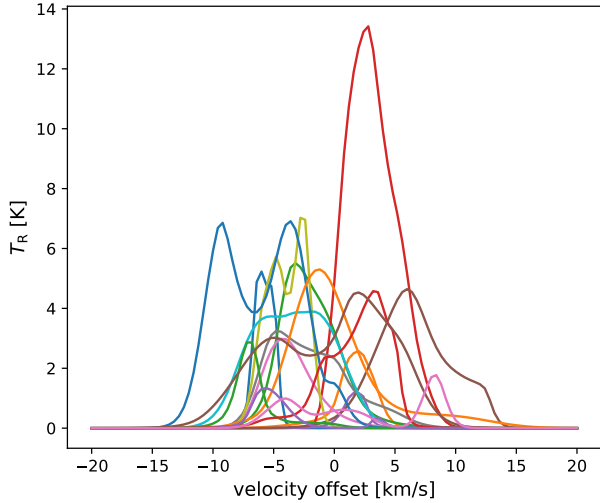


**Figure 18.** CO(1-0) spectra randomly drawn from the  $512 \times 512$  pixels in the  $Z' = 1$  run at  $t = 420$  Myr. Gas motion leads to a variety of spectrum profiles, including Gaussian-like, skewed, saturated, or even double-peaked.

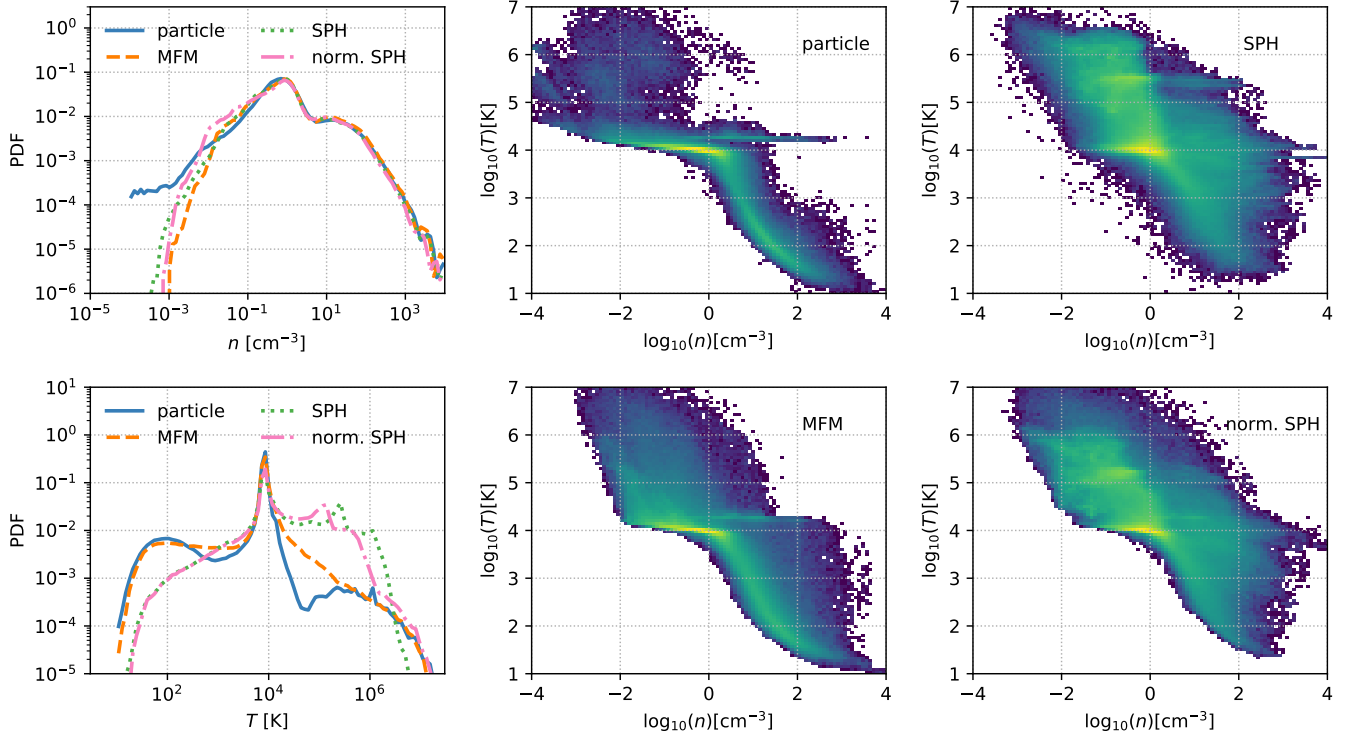


**Figure 19.** *Left panels:* Mass-weighted PDFs of hydrogen number density ( $n$ , upper panel) and temperature ( $T$ , lower panel) for the particle data, the standard SPH scheme (Eq. (D1)), the normalized SPH scheme (Eq. (D2)), and the MFM scheme (Eq. (D3)). *Middle and right panels:* “phase diagram” (heatmap of  $n$  vs.  $T$ ) for the particle data and the three interpolation schemes. The MFM scheme faithfully reproduces the distributions of  $n$  and  $T$ , while the two SPH schemes significantly overestimate  $T$ .